Key Points:
- Mesoscale resolution has a small effect on globally integrated carbon export (<2%), but local effects can be large (±50%)
- Improved representation of coastal jets and mesoscale turbulence limits export in regions where shelf-derived nutrients fuel production
- Deeper mixed layers with mesoscale resolution result in enhanced production in some regions

Supporting Information:
- Supporting Information S1
- Figures S1–S3
- Movie S1
- Movie S2
- Movie S3
- Movie S4

Correspondence to:
C. S. Harrison,
chsharri@ucar.edu

Mesoscale Effects on Carbon Export: A Global Perspective

Cheryl S. Harrison[1,2] ID, **Matthew C. Long**[1] ID, **Nicole S. Lovenduski**[2,3] ID, and **Jefferson K. Moore**[4]

[1]Climate and Global Dynamics Laboratory, National Center for Atmospheric Research, Boulder, CO, USA, [2]Institute of Arctic and Alpine Research, University of Colorado Boulder, Boulder, CO, USA, [3]Department of Atmospheric and Oceanic Sciences, University of Colorado Boulder, Boulder, CO, USA, [4]Department of Earth System Science, University of California, Irvine, CA, USA

Abstract Carbon export from the surface to the deep ocean is a primary control on global carbon budgets and is mediated by plankton that are sensitive to physical forcing. Earth system models generally do not resolve ocean mesoscale circulation ($\mathcal{O}(10-100)$ km), scales that strongly affect transport of nutrients and plankton. The role of mesoscale circulation in modulating export is evaluated by comparing global ocean simulations conducted at 1° and 0.1° horizontal resolution. Mesoscale resolution produces a small reduction in globally integrated export production (<2%); however, the impact on local export production can be large (±50%), with compensating effects in different ocean basins. With mesoscale resolution, improved representation of coastal jets block off-shelf transport, leading to lower export in regions where shelf-derived nutrients fuel production. Export is further reduced in these regions by resolution of mesoscale turbulence, which restricts the spatial area of production. Maximum mixed layer depths are narrower and deeper across the Subantarctic at higher resolution, driving locally stronger nutrient entrainment and enhanced summer export production. In energetic regions with seasonal blooms, such as the Subantarctic and North Pacific, internally generated mesoscale variability drives substantial interannual variation in local export production. These results suggest that biogeochemical tracer dynamics show different sensitivities to transport biases than temperature and salinity, which should be considered in the formulation and validation of physical parameterizations. Efforts to compare estimates of export production from observations and models should account for large variability in space and time expected for regions strongly affected by mesoscale circulation.

1. Introduction

The export of organic matter from the surface ocean to depth is an essential component of the global carbon cycle (Falkowski et al., 2000; Houghton, 2007). Termed the "biological pump," export acts to concentrate carbon in the deep ocean, sequestering it from the atmosphere and thereby exerting control on atmospheric CO_2 (e.g., Gruber & Doney, 2009). Export production (EP) is controlled by a complex set of physical, biological, and ecological processes. Fundamentally, net primary productivity (NPP), the creation of organic matter by phytoplankton, sets an upper bound on EP; thus, spatiotemporal variations in NPP manifest in changes in EP. Additionally, the fraction of NPP that is ultimately exported, termed the export ratio or "e-ratio," varies due to ecological factors such as phytoplankton community composition, trophic coupling, and aggregation processes (Burd & Jackson, 2009; Henson et al., 2015; Siegel et al., 2014). NPP and these ecological factors are sensitive to the physical mechanisms determining the character of the upper ocean environment. Specifically, the availability of limiting resources, light and nutrients, as well as ocean temperature are largely mediated by mixing and advection; thus, there is tight dependence between spatiotemporal distributions of EP and physical dynamics on planetary to local scales.

Earth system models (ESMs) are designed to study climate dynamics of the entire global coupled atmosphere-ocean-land-ice system under various forcing scenarios for thousands of years (Flato, 2011). Computational constraints necessitate model grids that are too coarse to explicitly resolve important processes driving climate, such as turbulent convection in clouds, crop coverage on land, and mesoscale turbulence in the ocean, all of which must be parameterized. As the mesoscale (roughly tens to hundreds of kilometers and days to weeks) dominates the kinetic energy spectrum in the ocean (Ferrari & Wunsch, 2009; Stammer, 1997) and has a large effect on fluxes of energy and carbon between the ocean and atmosphere

(Oschlies & Garçon, 1998; Small et al., 2008), much effort was put into developing parameterizations of the rectified effects of the eddying flow, with considerable success (Danabasoglu et al., 1994; Gent & McWilliams, 1990). However, it is impossible for these parameterizations to capture all processes relevant for carbon production and export, especially in highly dynamic regions. Moreover, coarse-resolution models do not resolve energetic mesoscale features, such as jets, not considered by eddy parameterizations. Thus, a question arises: is the skill of coarse-resolution representations of mesoscale processes mediating nutrient delivery and upper ocean dynamics sufficient to accurately simulate the biological pump? This consideration is especially timely, as great uncertainty exists in the observed regional and global magnitudes of the biological pump (e.g., DeVries & Weber, 2017; Henson et al., 2011), and much effort is underway by the ocean biogeochemical community to improve our understanding of physical and biological processes controlling carbon export (e.g., Siegel et al., 2016).

The role of mesoscale circulation in structuring primary production has been long recognized, with both vertical and horizontal transport known to exert strong controls (Abraham, 1998; Bracco et al., 2009; Martin, 2003; McGillicuddy et al., 1998). Interactions between fronts, eddies, and wind enhance vertical transport and mixing in the ocean (Hausmann et al., 2017; Koszalka et al., 2009; Oschlies, 2002; Small et al., 2008), bringing nutrients to the surface, affecting air-sea gas exchange, and injecting organic carbon downward (Gaube et al., 2013; Lévy, 2003; McGillicuddy et al., 2007; Omand et al., 2015; Song et al., 2016). Horizontal transport by filaments and eddies dominates the spatial structure of primary and secondary production (Abraham et al., 2000; Bracco et al., 2009), particularly in coastal systems (Harrison et al., 2013; Nagai et al., 2015), impacting carbon export processes (Lovecchio et al., 2017; Resplandy et al., 2012; Stukel et al., 2017). However, many uncertainties in the exact mechanisms and their regional importance remain (see recent reviews by McGillicuddy, 2016; Mahadevan, 2016). Indeed, cross correlations of observed global sea level and chlorophyll anomalies indicate a strong regional heterogeneity in the biological response to mesoscale variability (Gaube, McGillicuddy, et al., 2014). While observational and modeling studies present clear evidence that mesoscale and smaller-scale processes have large impacts on production and export, there is still much uncertainty in the net effects on the carbon cycle.

Modeling studies have shown that increasing resolution will increase vertical transport in some regions, in turn increasing nutrient fluxes over short timescales, but can lead to long-term changes in the biogeochemical background state that can decrease production over time (e.g., Gruber et al., 2011; Lévy, 2008; Lévy et al., 2001; Lévy, Iovino, et al., 2012; Oschlies & Garçon, 1998). Global implementations of eddy-resolving models have only recently become computationally feasible (e.g., Delworth et al., 2011; McClean et al., 2011). Adding a biogeochemical model requires additional computational effort and has been reported in only a few studies. Clayton et al. (2013, 2017) report on the changes in biodiversity and biogeochemistry between an eddy permitting (1/6°) and coarser-resolution (1°) ESM with a many-plankton ecosystem biogeochemistry model. Like previous regional models, they find increases in mixed layer depth (MLD) across the tropics and subtropics, corresponding to increases in vertical nitrate flux, driving greater primary production and plankton biomass. Clayton et al. (2017) also find decreases in primary production at subpolar latitudes, attributed to reductions in horizontal nutrient delivery due to changes in vertical mixing, somewhat similar to the one other regional study that compared mesoscale even finer resolution in a subpolar gyre (Lévy, Ferrari, et al., 2012). However, these two studies find different effects on plankton biomass with increasing resolutions, for reasons that remain unclear. Thus, while some progress has been made on assessing the regional and global impacts of resolving the mesoscale on production, many questions remain, and impacts on EP are largely unknown.

To explore the question of how the mesoscale impacts global and regional distributions of productivity and export, we compare two simulations of the Community Earth System Model (CESM), at eddy-resolving (0.1°), and non-eddy-resolving (1°) resolution. We consider net effects on global- and basin-scale means, and then we focus on regions of high carbon export in which resolved mesoscale circulation exhibits the largest effects. The physical mechanisms driving changes in productivity and export vary regionally, as do the net mesoscale effects. The various ways mesoscale turbulence affects production and export impacts best sampling strategies for these regions and demonstrates the need for parameterization improvement in global climate models.

2. Methods

2.1. Numerical Experiments

We analyzed global integrations conducted with the ocean and sea ice components of the CESM version 1 (CESM1) (Hurrell et al., 2013). One experiment was conducted at high-resolution (HI-RES) and another at low-resolution (LO-RES). Both integrations used the CESM ocean component, known as the Parallel Ocean Program (POP) version 2 (Smith et al., 2010). In the HI-RES experiment, POP was integrated on a global tripole grid with nominal horizontal spacing of 0.1° and 62 vertical levels, whereas in the LO-RES experiment, POP was integrated on a displaced pole grid with nominal horizontal spacing of 1° and 60 vertical levels. Both simulations included a prognostic sea ice model, the Community Ice Code version 4 (Hunke & Lipscomb, 2008), and are forced by the same atmospheric data set, the Coordinated Ocean_ice Reference Experiments (CORE) "Normal Year" repeating annual forcing (Griffies et al., 2009; Large & Yeager, 2004).

The models were integrated without biogeochemistry for 15 years, long enough to eliminate initial transients, initialized from rest with 0.5° × 0.5° World Ocean Circulation Experiment (WOCE) temperature and salinity (Gouretski & Koltermann, 2004). Biogeochemical tracers were initialized to observationally based climatologies where possible; where these were not available (such as dissolved iron and phytoplankton biomass), the model was initialized with fields interpolated from an existing, CORE-forced, 1° × 1° CESM case (Long et al., 2013). After enabling biogeochemistry, the model was integrated for 1 year, sufficient time for phytoplankton and zooplankton fields to stabilize and mesoscale variability in the tracer distributions to develop. Following this initialization, the models were integrated for 5 years and this is the output we analyze. HI-RES was integrated with a ~2 min timestep, while the LO-RES timestep was an hour; output was saved for both models at 5 day frequencies. The short time scale of the simulations does not allow for spinning up to steady state but does insure that model physics are acting on simulated nutrient fields that are still quite close to the observed distributions.

The critical difference between the LO-RES and HI-RES simulations relates to their representation of mesoscale dynamics. The HI-RES model simulates these explicitly and includes only biharmonic lateral diffusion for tracers and momentum. The LO-RES integration, by contrast, represents mesoscale effects using the well-known Gent & McWilliams (1990) parameterization of lateral mixing. The LO-RES experiment also includes a parameterization of the submesoscale, which simulates an overturning circulation in the surface mixed layer representing the restratifying effect of submeoscale mixed layer instabilities (Fox-Kemper et al., 2010). The vertical mixing scheme in both experiments was the K-profile parameterization of Large et al. (1994); the models have the same vertical resolution.

Ocean biogeochemistry in both HI-RES and LO-RES was simulated by the CESM1 Biogeochemical Elemental Cycle (BEC) model (Moore et al., 2013). BEC includes three explicit phytoplankton functional groups (diatoms, diazotrophs, and picophytoplankton/nanophytoplankton) and one implicit group (calcifiers) subject to multiple nutrient limitation (N, P, Si, and Fe) (Moore et al., 2004). The model includes a single zooplankton class that grazes the different phytoplankton at specific rates, with routing of grazed material that varies by prey type (Doney & Ducklow, 2006; Moore et al., 2004). Iron delivery to the ocean is simulated following Moore and Braucher (2008); iron inputs include specified atmospheric deposition (monthly climatology) and a sedimentary source applied using subgrid-scale bathymetry.

Sinking particulate matter is represented implicitly following Armstrong et al. (2002); sinking material is either free or associated with ballasting materials: mineral dust, biogenic calcite, or silica (Moore et al., 2004) and is instantaneously distributed with depth following an exponential flux attenuation function. Particulate organic carbon (POC) is produced from phytoplankton directly via linear (as a function of biomass) mortality, as well as quadratic aggregation (diatoms and small phytoplankton). Additionally, grazing by zooplankton produces POC via egestion, sloppy feeding and through zooplankton mortality, which has both a linear and nonlinear component. Thus, the POC production (POC_{prod}) can be written as follows:

$$POC_{prod} = SP_{agg} + SP_{loss}^{POC} + Diat_{agg} + Diat_{loss}^{POC} + G_{SP}^{POC} + G_{Diat}^{POC} + G_{Diaz}^{POC} + Z_{loss}^{POC}, \qquad (1)$$

where SP are small (pico/nano) phytoplankton, Diat are diatoms, Diaz are diazotrophs, G is grazing, Z is zooplankton, loss is mortality, and agg is aggregation (see also Lima et al., 2014). The diazotroph class in BEC only contributes to POC through zooplankton grazing; because diazatroph biomass is low, this contribution is minimal.

Global solutions of the coarse-resolution CESM ocean component including the BEC model have been validated extensively against observations (e.g., Doney et al., 2009; Lima et al., 2014; Long et al., 2016, 2013; Moore & Braucher, 2008; Moore et al., 2002, 2013, 2004). Applications involving BEC integrated at high resolution are limited but include regional studies in the North Atlantic and California Current (Anderson et al., 2011; Gaube & McGillicuddy, 2017; McGillicuddy, 2014; Renault et al., 2016). The HI-RES model solution presented here generally compares favorably to observations (Figures S1 and S2). The simulated large-scale chlorophyll distributions in HI-RES show realistic global structure, but chlorophyll tends to be too high in oligotrophic systems and generally too low at high latitudes and along coastlines (Figure S1, supporting information). MLDs are much improved in the HI-RES model integration relative to LO-RES (Figure S2). In the next section we proceed with a detailed analysis of the mechanisms controlling EP in these two simulations.

2.2. Analysis

Organic carbon can be transported from the surface to depth via sinking particulates or the advection of dissolved material (Carlson et al., 1994; Omand et al., 2015; Turner, 2015). The effective boundary between the surface and deep ocean (i.e., the depth at which carbon is considered exported) has various definitions (Buesseler & Boyd, 2009; Lima et al., 2014; Siegel et al., 2014) but is often approximated as 100 m (e.g., Henson et al., 2015). We consider EP defined as the POC flux at 100 m, recognizing that this ignores variations in the euphotic and MLDs. Only 2% of the global POC production occurs below 100 m in the HI-RES simulation, indicating that the error due to this simplification is small for this model integration. We also neglect for this study the vertical transport of dissolved organic carbon. While dissolved organic carbon export accounts for an estimated 25% of the total carbon export out of the euphotic zone (Letscher et al., 2015; Lindsay et al., 2014), the sinking flux strongly dominates the flux to the deep ocean, especially outside of subtropical gyres (Letscher et al., 2015).

NPP is the rate of carbon fixation integrated over the ocean surface layer (top 100 m) and includes contributions from the three phytoplankton types. The export ratio (e-ratio) is the proportion of NPP that is exported as sinking POC flux at 100 m: e-ratio = EP/NPP.

We develop inventories of total iron in the upper ocean, which includes bioavailable, dissolved inorganic iron (Fe), and iron in organic pools:

$$\text{Total iron} = \text{Fe} + \text{spFe} + \text{diatFe} + \text{diazFe} + \text{zooFe} + \text{DOFe}, \tag{2}$$

where spFe, diatFe, diazFe, and zooFe are the iron contained in the various plankton classes and DOFe is iron in the dissolved organic pool. Total iron was integrated over the top 100 m.

We define a seasonality index (SI) as SI $= (6 - t_{\frac{1}{2}})/6$, where $t_{\frac{1}{2}}$ is the production half time, the minimum time in months for half of the annual production to be generated, adapted from Berger and Wefer (1990). For regions of constant, steady production, the half time will be 6 months, while for high latitudes the half time is less than 1 month due to the short growing season; thus, SI is between 0 and 1, with 0 being no seasonality (year-long growing season with constant production) and 1 being maximum seasonality (short growing season). The SI metric is calculated for EP using the annual monthly climatology in the HI-RES simulation.

Open-ocean polynyas (ice-free regions) tend to form in the Weddell Sea, both in observations and in many coupled and forced ocean models, greatly enhancing local vertical mixing and air-sea fluxes (de Lavergne et al., 2014; Downes et al., 2015). A polynya forms in the HI-RES simulation, growing in horizontal extent each model winter; no polynya forms in the LO-RES simulation though the atmospheric forcing is identical. This region is excluded from the regional integrals used to compare the two simulations.

3. Results

3.1. Distributions and Differences Between Simulations

The geographical distribution of carbon export is strikingly similar between the two model solutions, reflecting comparable nutrient delivery to the euphotic zone over much of the ocean (Figure 1). Annual mean POC EP in CESM is elevated across equatorial regions in the Indian, Atlantic, and Pacific Oceans, extending into the tropics in the Indian, eastern Atlantic, and far eastern Pacific Oceans. Export is low in all the subtropical gyres. At southern midlatitudes, export is high in the South Atlantic around the Argentine Basin, extending across the Atlantic to Africa. Export is also high all across the northern flank of the Antarctic Circumpolar Current (ACC) with particularly high values south of Australia and New Zealand, and around the Kerguelen Plateau to the west. In the North Pacific, export is moderate in the midlatitude central region and high west of mainland
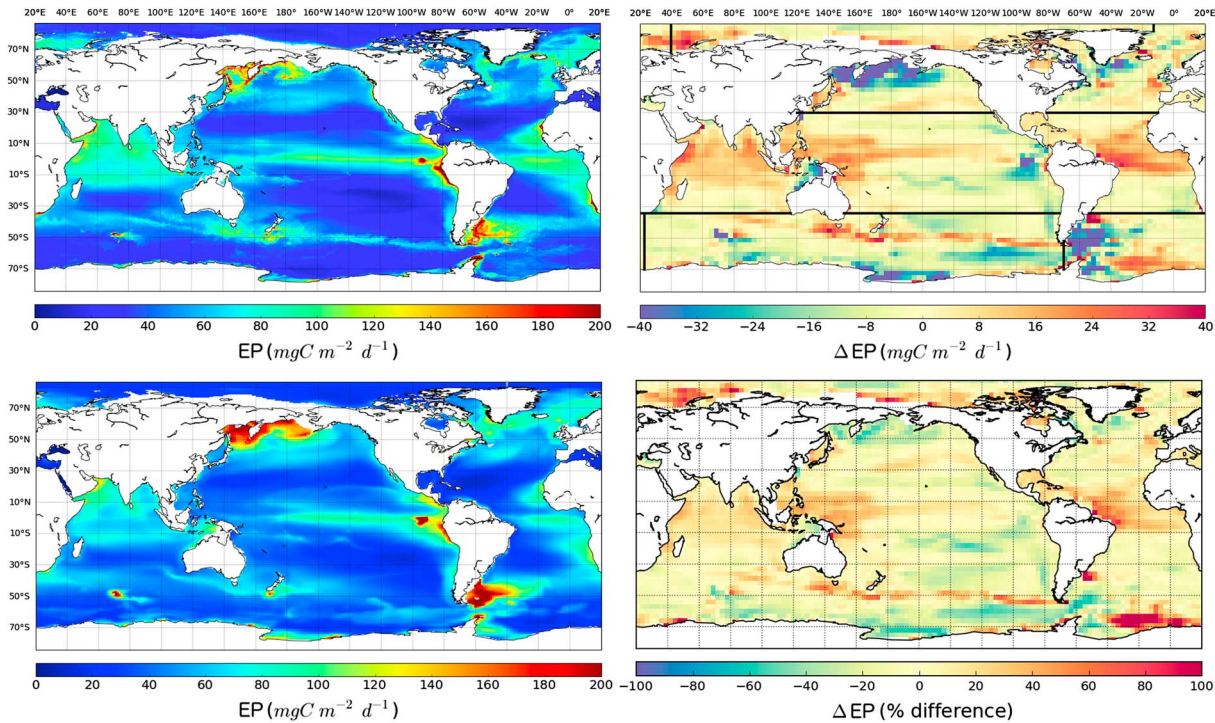
Figure 1. Annual mean of carbon export production (EP) in both simulations, top left is HI-RES, bottom left is LO-RES, top right is difference (HI-RES−LO-RES), and bottom right is percent difference relative to LO-RES, with the last two plots remapped to 3°. Black lines show basin boundaries used in Table 1.

Alaska, extending from coastal shelf regions in the Bering and Okhotsk Seas and around the Aleutian and Kuril Islands. In the North Atlantic, export is moderate at midlatitudes, somewhat similar to the distribution in the North Pacific. North of this, export is high near Greenland and east of Iceland extending from the Iberian Peninsula to high latitudes. Export is high in all the eastern boundary upwelling regions (e.g., off California and Peru), with the exception of the Iberian Peninsula.

The distribution of EP and e-ratio in CESM is similar to satellite-based models (Figure 2; DeVries & Weber, 2017; Siegel et al., 2014), and the difference between satellite-based estimates is comparable to the difference between the model integrations and the satellite-based models. For example, relative to Siegel et al. (2014), export in CESM is higher in the coastal North Pacific, more similar to DeVries and Weber (2017). Satellite-based export is higher near the Amazonian outflow and across many coastal regions; in both CESM simulations, riverine nutrient inputs are not included and coastal upwelling circulation is not well simulated, even at 0.1°

Table 1
Basin and Globally Integrated Export Production for the HI-RES (HR) and LO-RES (LR) Model Simulations

Region	EP (Pg C yr⁻¹)				NPP (Pg C yr⁻¹)				e-ratio			
	HR	LR	Diff	% Diff	HR	LR	Diff	% Diff	HR	LR	Diff	% Diff
Arctic	0.072	0.067	0.005	7.7	0.51	0.41	0.09	24	0.307	0.286	0.021	0.07
N Pacific	0.58	0.67	−0.09	−13	3.63	3.79	−0.17	−4.4	0.174	0.184	−0.011	−0.06
N Atlantic	0.47	0.49	−0.02	−4.5	2.96	3.04	−0.08	−2.6	0.175	0.174	0.001	0.01
Trop. Pacific	1.92	1.93	−0.01	−0.62	16.8	16.6	0.26	1.5	0.110	0.113	−0.003	−0.03
Trop. Atlantic	0.86	0.77	0.09	12	7.33	6.56	0.77	12	0.114	0.112	0.001	0.01
Indian	1.07	0.97	0.10	9.9	9.10	8.29	0.80	9.7	0.124	0.123	0.001	0.01
WSouthern Ocean	0.53	0.59	−0.06	−10	2.73	2.95	−0.22	−7.5	0.208	0.207	0.001	0.00
ESouthern Ocean	1.09	1.21	−0.11	−9.4	6.63	7.19	−0.56	−7.8	0.170	0.175	−0.004	−0.02
Total	6.60	6.71	−0.11	−1.6	49.7	48.8	0.9	1.8	0.144	0.146	−0.002	−0.02

Note. Difference (Diff) is HI-RES-LO-RES; percent difference (% Diff) is relative to LO-RES. Region boundaries are shown in Figure 1. Note that basin- and global-scale e-ratios are the area weighted means of the local e-ratio, not the ratio of integrated net primary productivity (NPP) and export production (EP).
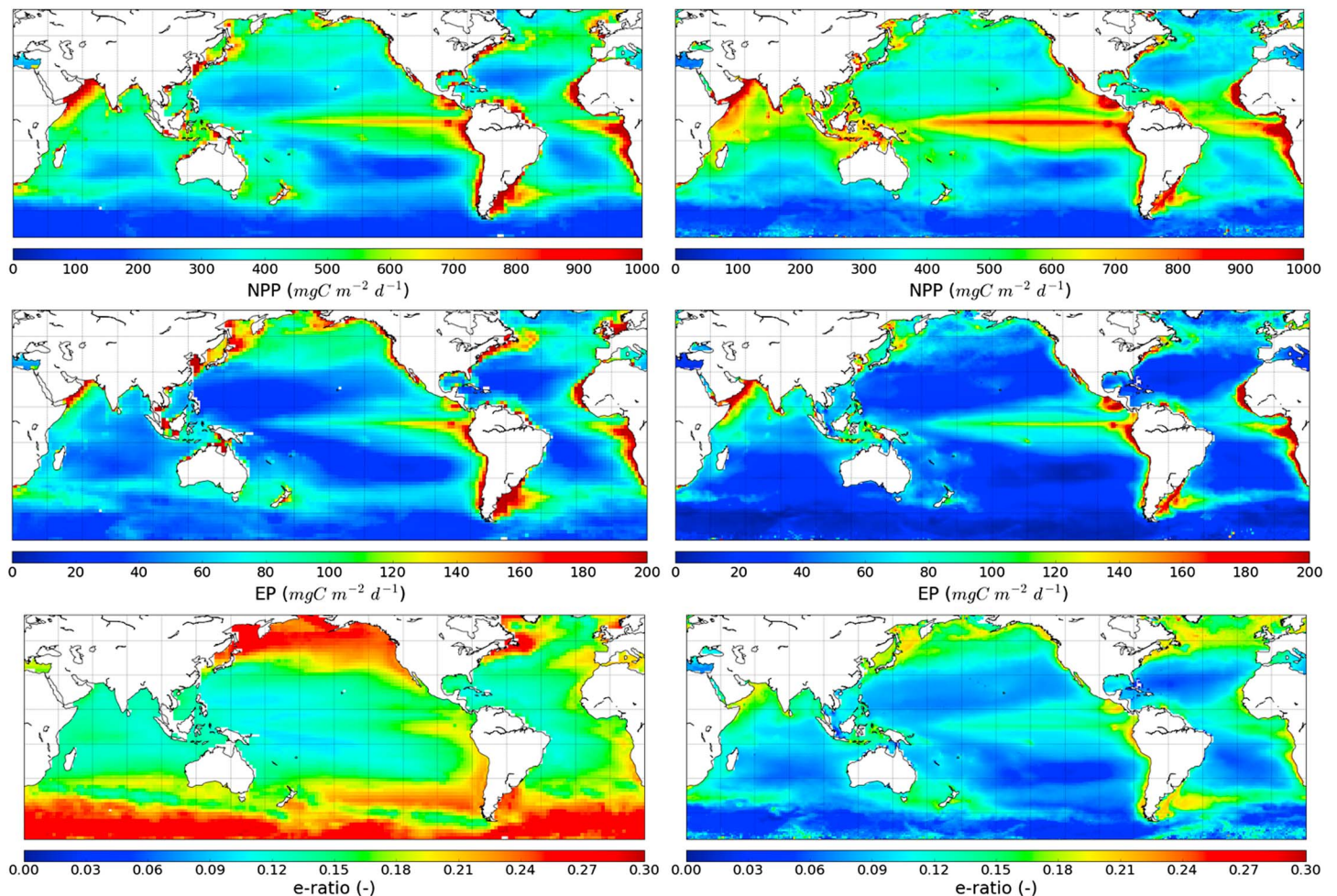
Figure 2. Results from the satellite-based food web models of DeVries and Weber [DeVries and Weber (2017)] (left column) and Siegel et al. [Siegel et al. (2014)] (right column). Shown are net primary productivity (NPP) (top row), export production (EP) (center row), and e-ratio (bottom row). For the Devries and Weber data, NPP is the mean of the Vertically Generalized Production Model and Carbon-based Production Model NPP estimates (see DeVries and Weber [DeVries and Weber (2017)] for details), and the mean of EP and the e-ratio are taken over the 12 model versions. EP is taken at the estimated euphotic depth for both models.

resolution (Small et al., 2015; Wang et al., 2014). It should be noted that satellite-based export proxies are based on ocean color-derived estimates of Chl, which are known to have biases at high latitudes (e.g., Johnson et al., 2013). These satellite-based models, similar to ESMs, make a number of assumptions about the food web and export efficiency of each related detrital component, and the in situ observations used to constrain them are limited.

Estimates of annual global EP range from 3 to over 10 Pg C yr^{-1} (DeVries & Weber, 2017). Globally integrated, annual mean EP in HI-RES (6.60 Pg C yr^{-1}) is only slightly lower than LO-RES (6.71 Pg C yr^{-1}), a difference of 1.6%, and consistent with previous integrations of CESM (Lima et al., 2014; Lindsay et al., 2014). As a point of comparison, the range of annual mean, global EP in CESM simulations forced by the interannually varying CORE-2 data set (Danabasoglu et al., 2014) is 0.4 Pg C yr^{-1} (not shown), 4 times the difference between the two simulations. On the basin scale, the difference in EP between HI-RES and LO-RES varies with latitude, with compensating effects between the tropics and high latitudes (Table 1). Export is ∼10% greater in HI-RES in the tropical Atlantic and Indian Oceans but similar in the tropical Pacific. At high latitudes, regionally integrated export is ∼10% lower in the Southern Ocean and North Pacific and more similar in the Arctic and North Atlantic Basins. The basic similarity of globally integrated and basin-scale EP in the two models suggests that resolved eddies do not fundamentally change the nature of the biogeochemistry simulation over the 5 year simulation.

The LO-RES and HI-RES solutions were remapped to 3° to facilitate comparison of spatial patterns. We display both the difference (HI-RES minus LO-RES) and the percent difference of the HI-RES model from the LO-RES
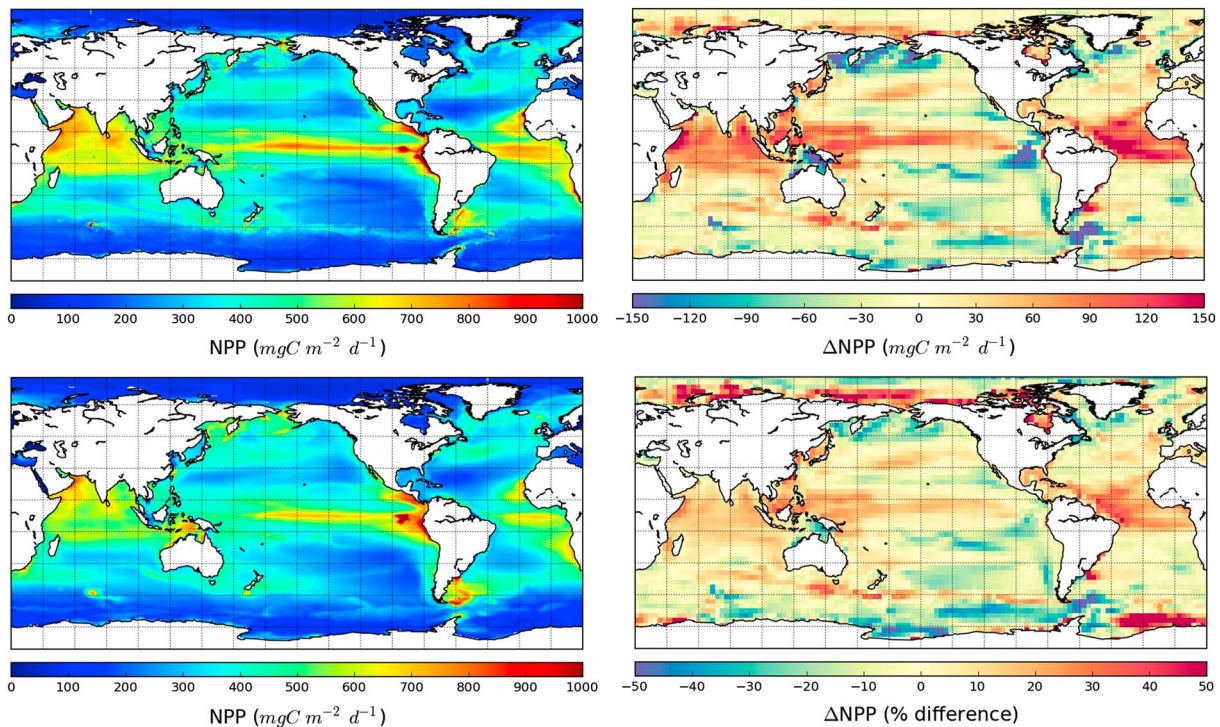
Figure 3. As in Figure 1 but for net primary productivity (NPP).

(Figure 1). While EP at the basin scale is comparable between the two solutions, local differences are large, particularly in areas with high EP. In the two regions with the most intense export in the model, the Patagonian Basin and North Pacific, the HI-RES solution has up to 50% lower EP. In areas within the tropics, by contrast, the HI-RES model has upward of 50% higher export than LO-RES.

Differences in EP can be considered to manifest from differences in NPP (Figure 3) and the export ratio (Figure 4); that is, EP = NPP × e-ratio, which leads to the linearizion

$$\Delta EP = \Delta NPP \times \text{e-ratio} + NPP \times \Delta \text{e-ratio}, \qquad (3)$$

where Δ is the difference between the two simulations. Across the tropics, the greater EP in HI-RES is primarily attributable to NPP, both of which are about 50% higher in HI-RES, while differences in the e-ratio are generally small. In regions where EP is lower in HI-RES, differences in both NPP and the e-ratio contribute, for example, in the North Pacific and Antarctic outside of the Weddell Sea (where the polynya forms in HI-RES); however, lower NPP is responsible for most of the EP difference (e.g., ΔNPP = −40% in the North Pacific relative to Δe-ratio = −20%). In the model, e-ratio tends to vary in concert with export, so that regions with higher productivity and export at higher resolution also have higher export ratios, and vice versa, highlighting the nonlinearity (positive concavity) in the NPP to EP relationship in CESM-BEC.

The annual mean MLD has large regional differences between the two simulations, in some regions over ±50% (Figure 5). Mixed layers are deeper in the HI-RES simulation across the tropics and in western boundary current extension regions (e.g., Gulf Stream). In the Southern Ocean, the locations of deepest mixing differ between the LO-RES to HI-RES model simulations, with deeper mixed layers along a more narrowly confined region in the Subantarctic in the HI-RES solution. Many regions with deeper MLDs in the HI-RES simulation also correspond to regions of greater NPP and EP, for example, western boundary extensions and some sectors of the tropical oceans. The positive spatial correlation of ΔMLD with ΔEP and ΔNPP is particularly high across the Southern Ocean.

Maps of the most limiting nutrient are largely similar between the two solutions (Figure 6). Iron is limiting production across most of the high-latitude oceans and in the equatorial Pacific, with limitation extending closer to the coasts in HI-RES. Nitrate is most limiting in the Indian Ocean and across the subtropical gyres, with the exception of the North Atlantic, where phosphate is limiting. The regions of highest regional
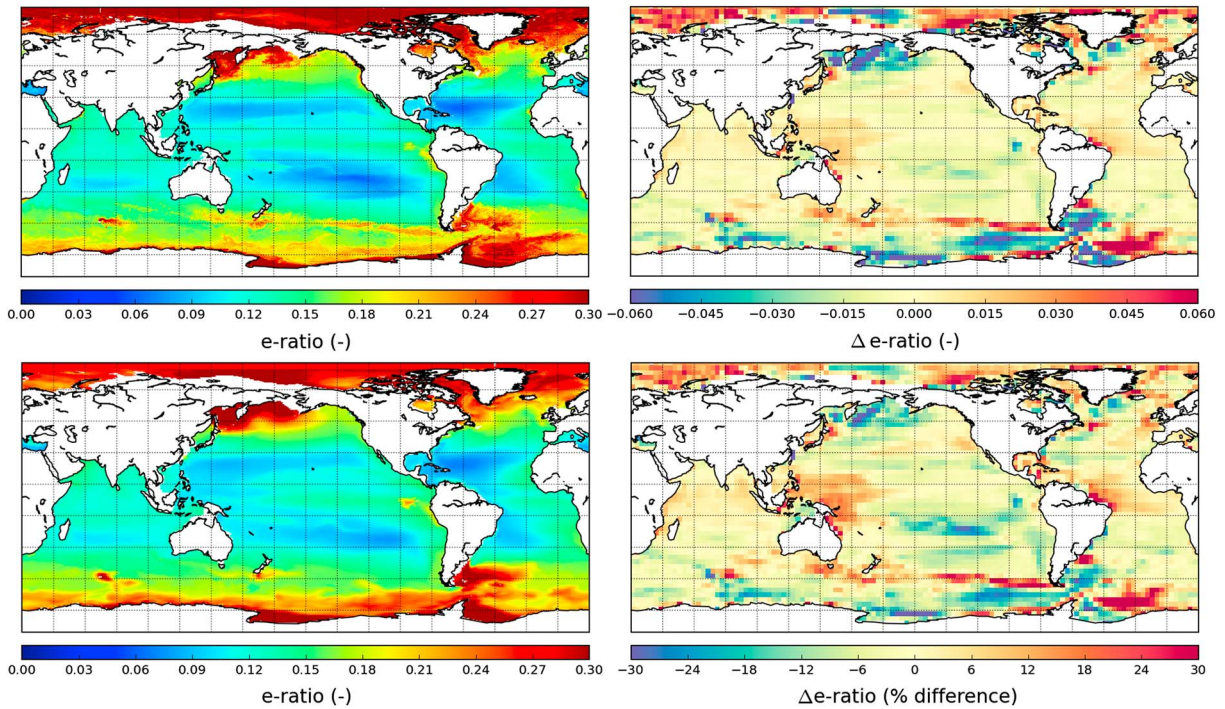
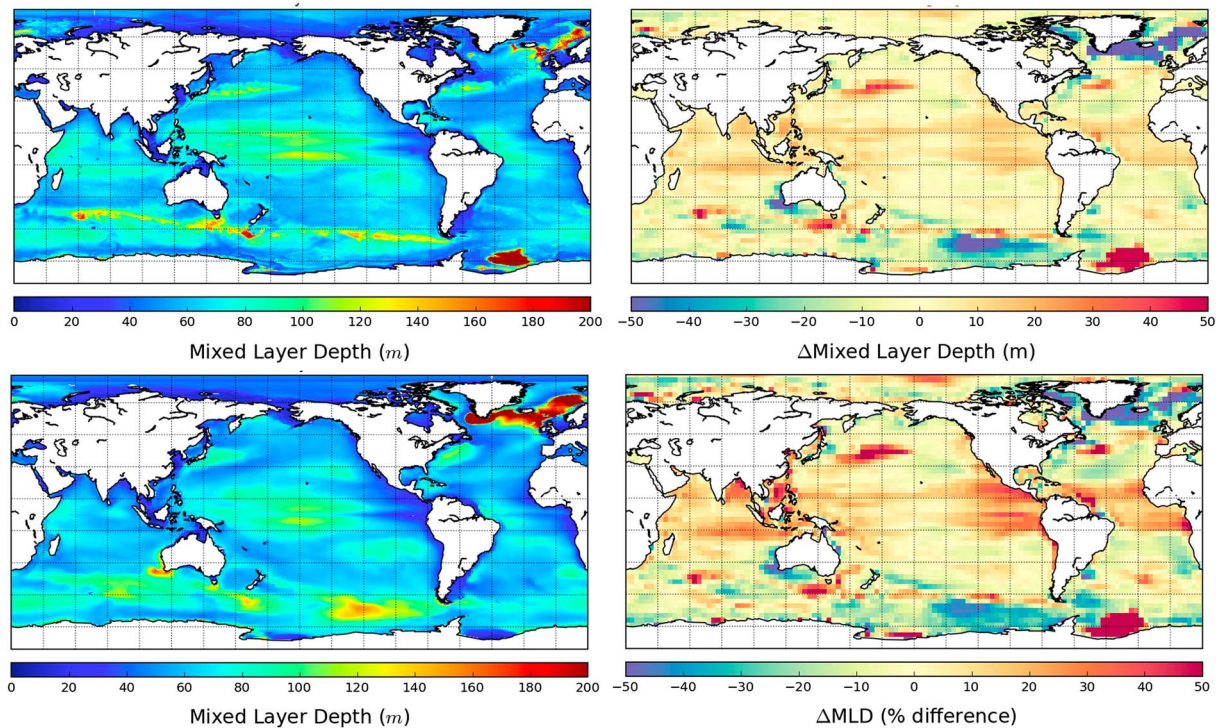**Figure 4.** As in Figure 1 but for export ratio (e-ratio = export production/net primary productivity).

Figure 5. As in Figure 1 but for mixed layer depth (MLD). MLD was taken from the model output average MLD (HMXL; Large et al., 1997).
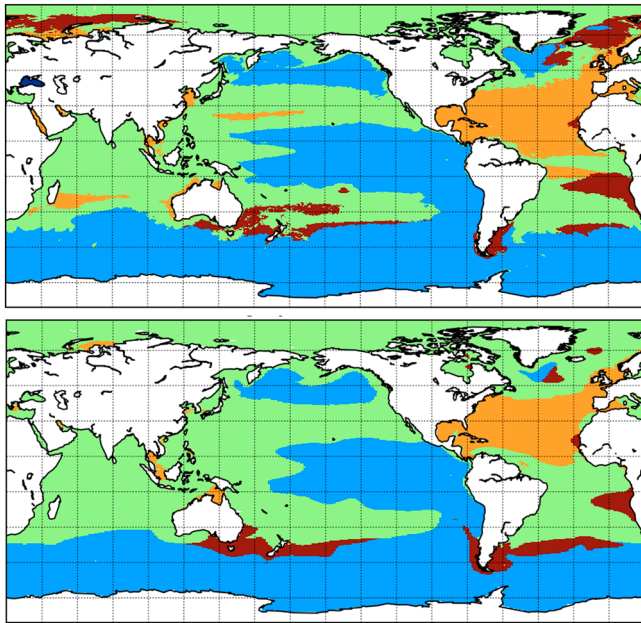
Figure 6. Annual mean nutrient limitation comparison for diatoms: top is HI-RES, bottom is LO-RES. Blue is iron, green is nitrate, orange is phosphate, and red is silica. Limitation maps were taken from the annual mean of the limitation terms, using the most limiting factor for the phytoplankton type in question. Limitation maps for small phytoplankton are similar, with silica limitation replaced largely by iron limitation (not shown).

export flux in the model—the Southern Ocean, tropical Pacific, and North Pacific—are all iron limited. Notably, ∼40% of the global carbon export flux occurs in persistently iron-limited regions (39.8% in LO-RES and 41.2% in HI-RES), indicating the strong control delivery of iron has on global productivity and export.

3.2. Seasonality and Variance of Export and E-Ratio

Seasonality of productivity, combined with the intensity of the mesoscale flow, impacts the degree to which resolving the mesoscale affects EP. EP is more seasonal at high latitudes (Figure 7), following from light limitation restricting the growing season. For example, in the high-export region associated with the Subantarctic Front, the annual export is accomplished over just a few months, associated with the austral spring bloom; here the EP half time is 1 month and the SI is 5/6. In the Patagonian Basin of the South Atlantic, the annual export occurs over less than 4 months, so that SI = 4/6, with a similar value in the North Pacific and North Atlantic Basins. In contrast, EP is much more constant across the tropics, so that SI = 0 in regions of the tropical Pacific and Atlantic sectors, indicating that productivity and export are continuous throughout the year. Regions with high seasonality in EP are more impacted by year-to-year internal variability of the mesoscale flow.

Many regions of high EP seasonality are also associated with a large, spatially patchy standard deviation in the annual mean e-ratio (Figure 7). The atmospheric data sets used to force the model comprise an annually repeating cycle; however, internal variability of the ocean in energetic areas is significant, manifesting in differences in the locations of eddies and meanders from year to year. These variations, due to resolving mesoscale turbulence, affect the distribution of production and export, particularly in regions where the export season is short. Regions where intense production occurs over a short growing season are more likely controlled by details in the spatial structure of the eddying flow, explored more in the next section.

3.3. Physical Drivers of Export Changes

We have demonstrated that differences in EP between high- and low-resolution solutions are primarily attributable to differences in NPP, with secondary and correlated effects due to differences in the e-ratio (Table 1). The impact of resolution on NPP and EP depends on which nutrient limits productivity and the role of advection in mediating its delivery to the euphotic zone. We find that effects can be roughly grouped into two categories: (1) diminished production due to less horizontal transport of a limiting nutrient at high resolution and (2) increased production driven by vertical processes leading to greater upward nutrient fluxes at high resolution. Additionally, many regions with large differences in EP between high- and low-resolution solutions are associated with regions of intense variability, so that mesoscale circulation strongly structures biogeochemical responses in both space and time. Below we examine in detail how EP changes with mesoscale resolution in a few regions of interest, where the difference in EP is greatest between the two model simulations.

3.3.1. Horizontal Transport

A number of regions in our modeled ocean display EP that is both intense and sensitive to horizontal transport processes: the North Pacific, the Argentine Basin in the South Atlantic, and around islands in the Southern Ocean and eastern equatorial Pacific. In these regions, iron is the most limiting nutrient (Figure 6), consistent with observations (Moore et al., 2002, 2013). Here lateral transport of iron is known to exert a strong control on biological production (d'Ovidio et al., 2015; Misumi et al., 2011; Qin et al., 2016; Smetacek et al., 2012). Bioavailable iron is supplied to the ocean by sedimentary sources and atmospheric dust deposition, parameterized in CESM as fluxes that vary in space but are constant (sediment flux) or climatological (dust) in time (Moore & Braucher, 2008; Moore et al., 2002). We show below that the mesoscale flow in continental shelf regions, or its parameterization, greatly affects the spatial distribution of production and export in iron-limited regions.
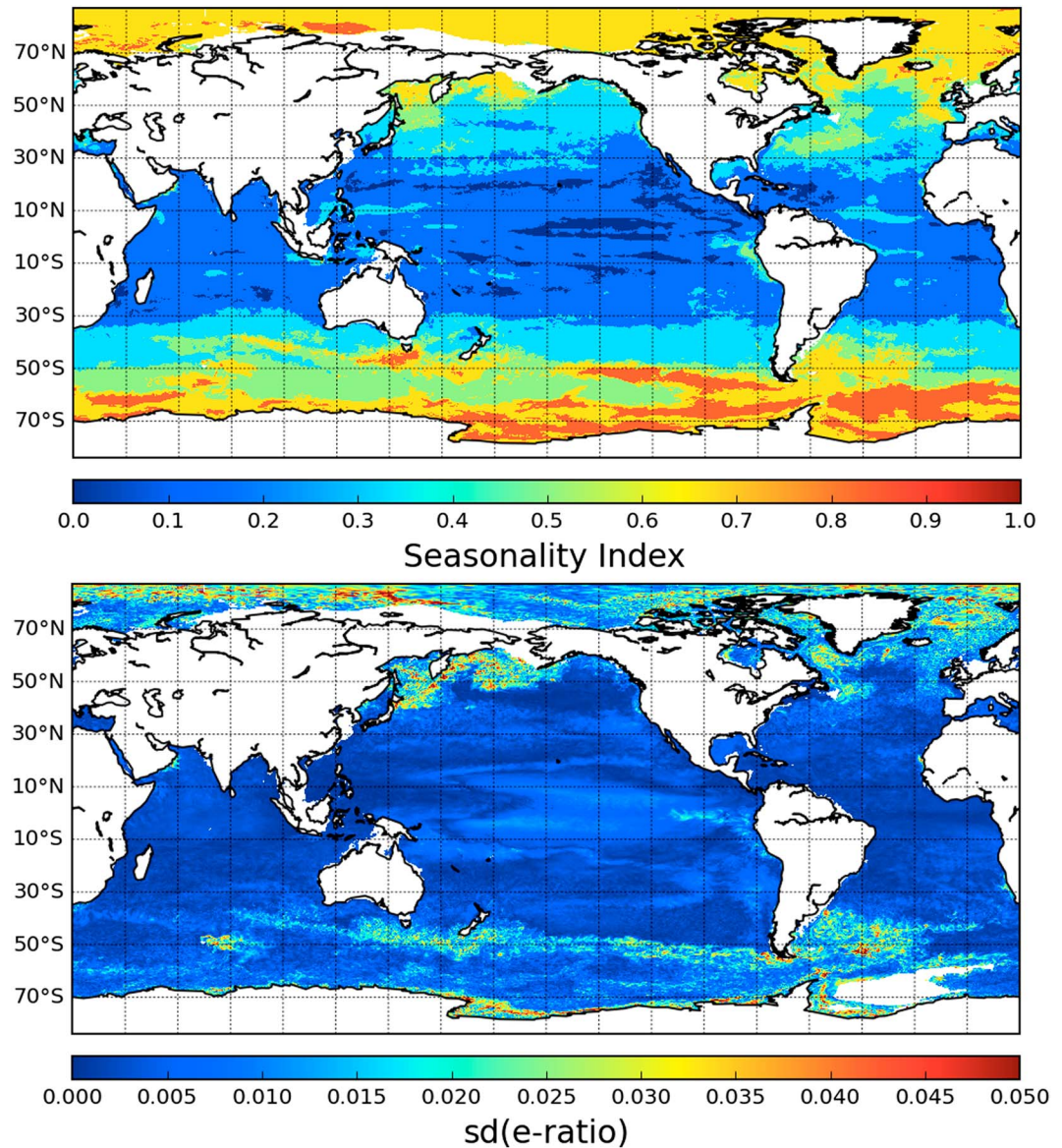
Figure 7. Seasonality index for export production (top) and standard deviation of annual export ratio (bottom), both for the HI-RES simulation.

In ESMs, unresolved horizontal stirring and mixing in the surface ocean is parameterized as a diffusive tendency that depends on the local gradient of the tracer to be transported, so that the time rate of change of any tracer concentration C at any point can be written as follows:

$$\frac{\partial C}{\partial t} = -\nabla \cdot (\mathbf{u}\,C) + \nabla \cdot (\kappa \nabla C) + F_C(\mathbf{x}).\tag{4}$$

The first term on the right-hand side represents advection of the tracer (and its gradients) by the ocean currents, and the last term F_C the forcing or sources and sinks for each tracer. In ESMs, the second term is parameterized subgrid-scale mixing, modeled as tracer diffusion, such that tracer gradients are smoothed out over time and space at a rate dependent on the "eddy diffusivity" κ and the tracer gradient (Danabasoglu et al., 1994; Gent & McWilliams, 1990; Redi, 1982). Usually, the parameterized diffusivity κ is the same for all tracers, both passive and dynamic.

The parameterized diffusive tendency is formulated to represent the net effect of eddies. However, in some regions of the ocean both the mean and fluctuating components of the realistic flow will act to intensify
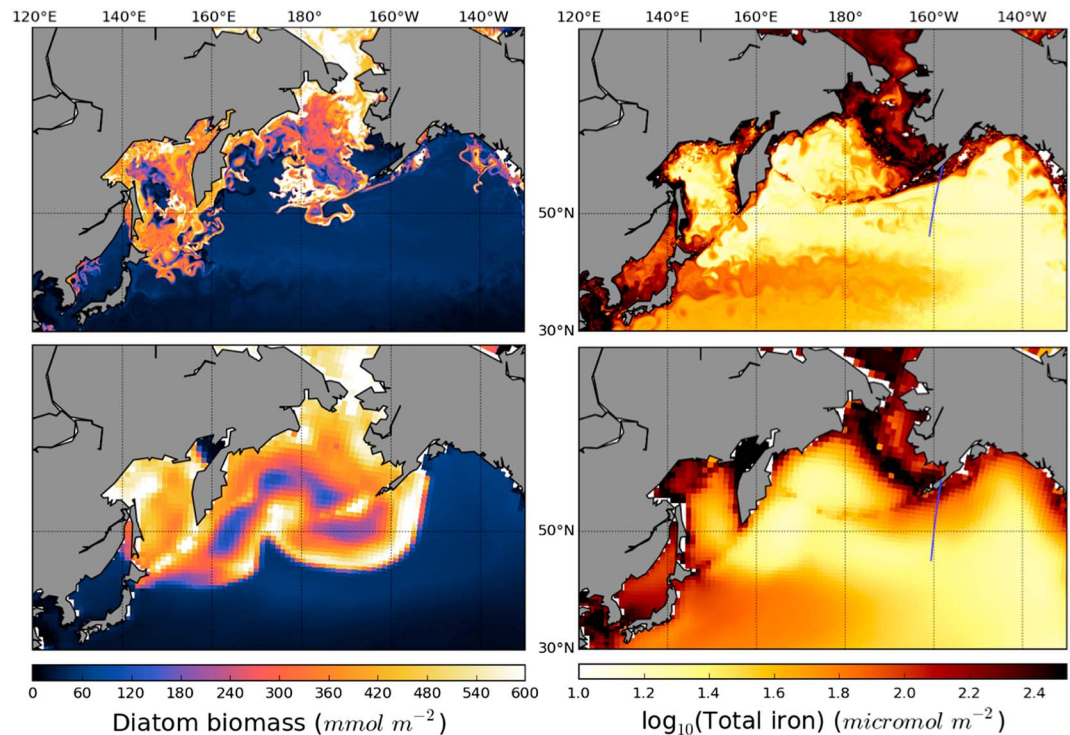
Figure 8. Comparison of summer diatom bloom in the North Pacific on 8 August for both simulations. Left is diatom biomass, and right is total iron, both integrated over the top 100 m. Top is HI-RES, and bottom is LO-RES. Blue lines indicate transects shown in the following figure. Resolution of coastal mesoscale circulation, including coastal jets, limits off-shelf transport of iron, and the resulting biological response.

gradients, especially over the time scales relevant for biogeochemical reactions (Abraham, 1998; Harrison et al., 2013). It is in these regions that the subgrid-scale eddy parameterization leads to spreading out of tracer gradients more in the coarse-resolution model. Below we highlight two regions where iron transport and production are greatly enhanced by the eddy parameterization: the North Pacific and South Atlantic.

3.3.1.1. North Pacific

The North Pacific subpolar gyre is one of the regions of greatest EP in both models and satellite-based estimates (Figure 2; DeVries & Weber, 2017; Dunne et al., 2005; Henson et al., 2012; Laufkötter et al., 2016; Lima et al., 2014; Siegel et al., 2014). In both the HI-RES and LO-RES solutions, production in the North Pacific is dominated by a summer diatom bloom. This region is largely iron limited (Figure 6); much of the regional iron supply is provided by continental shelf sediment sources (Misumi et al., 2011). We find that resolution of the coastal circulation and the associated turbulent flow exerts a large control on patterns of production and export through mediating the nature of this supply.

Resolution of coastal jets south of the Aleutian Islands and east of the Kamchatka Peninsula limits off-shelf transport of coastally released iron (Figure 8). For example, at high resolution the Alaskan Stream south of the Aleutians is a narrow, swift, and deep jet, reaching speeds of over 30 cm s^{-1} and extending tens of kilometers off the shelf break (Figure 9), consistent with regional modeling studies and observations (cf. Durski et al., 2016). In HI-RES, iron is retained along the coast on the inshore side of this coastal jet, consistent with the region of highest velocity shear acting as a transport barrier, retaining material near the coast (Harrison & Siegel, 2014). The LO-RES model does simulate a coastal jet; however, it is much weaker and wider, and iron is distributed diffusely across it. Iron transport in HI-RES, by contrast, is largely constrained to within vortices and filaments along the shelf break, where the coastal currents become unstable and allow off-shelf transport, while in LO-RES iron is more diffusely and uniformly distributed away from the coasts (Figures 8 and 9). The HI-RES results are consistent with observations and regional models, which show effective offshore iron transport occurs mainly in association with large mesoscale eddies (Combes et al., 2009; Fiechter & Moore, 2012; Johnson et al., 2005). This restriction of iron in HI-RES decreases the overall intensity and spatial extent
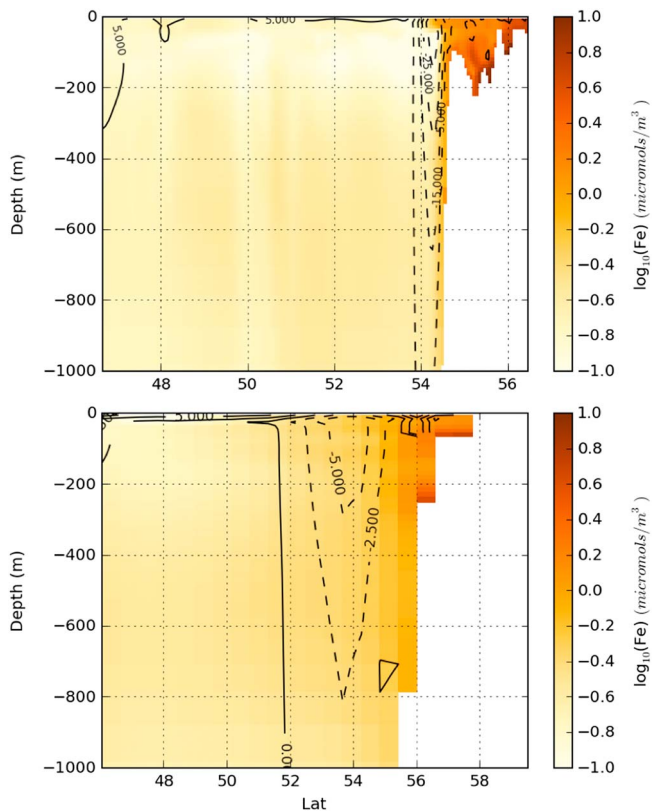
Figure 9. Off-shelf transects of iron concentration around 160°W in the North Pacific, along the blue lines in the previous figure. Contours are cross-transect velocity (cm/s), dashed lines indicate into the page, roughly westward. In the HI-RES model, iron is restricted off shelf of the coastal jet.

of the bloom while increasing the spatial variance (Figure 8, Movie S1), whereas delivery of sedimentary iron to a wider spatial area in LO-RES relieves limitation, expanding the bloom in space.

The net effect of resolving the mesoscale flow is that the regional depth-integrated total iron concentration in HI-RES is over 50 times lower than in LO-RES in many areas off the shelf (Figure 8), leading to a reduction in annual NPP, EP, and e-ratio in the North Pacific of 30–50% in HI-RES (Figures 1 and 3–5). This result can be related to changes in the probability distributions of these quantities (Figure 10). The annual mean NPP probability distribution is shifted to lower values at higher resolution (median = 313 mg C m^{-2} d^{-1} in HI-RES versus 410 in LO-RES), with a corresponding shift in the EP distribution (median = 60 mg C m^{-2} d^{-1} versus 98). As the iron-fertilized, diatom-dominated bloom has a higher export ratio than the rest of the subpolar gyre, the e-ratio probability distribution is skewed to lower values in HI-RES due to the smaller spatial extent of the bloom (median = 0.19 versus 0.24), even though the joint distributions of NPP and EP are largely consistent for the two simulations (Figure 10).

In the subpolar North Pacific, we can discern that horizontal stirring processes are driving patterns of production and export, as opposed to mesoscale circulation mediated vertical processes such as eddy-wind interaction (Gaube, Chelton, et al., 2014; Song et al., 2015); here the limiting factor, iron, is minimal below the euphotic zone and the dominant iron gradient is horizontal (Figure 9). Changes in the horizontal distribution of iron vary from year to year driven by variations in the mesoscale flow, resulting in a high standard deviation of the local export ratio (Figure 7); these variations effect the locations and strength of local production and export patterns. Within this complex and varying flow, production is sometimes highest within eddies, sometimes high around their peripheries, and in general highly variable in both space and time (Movie S1).
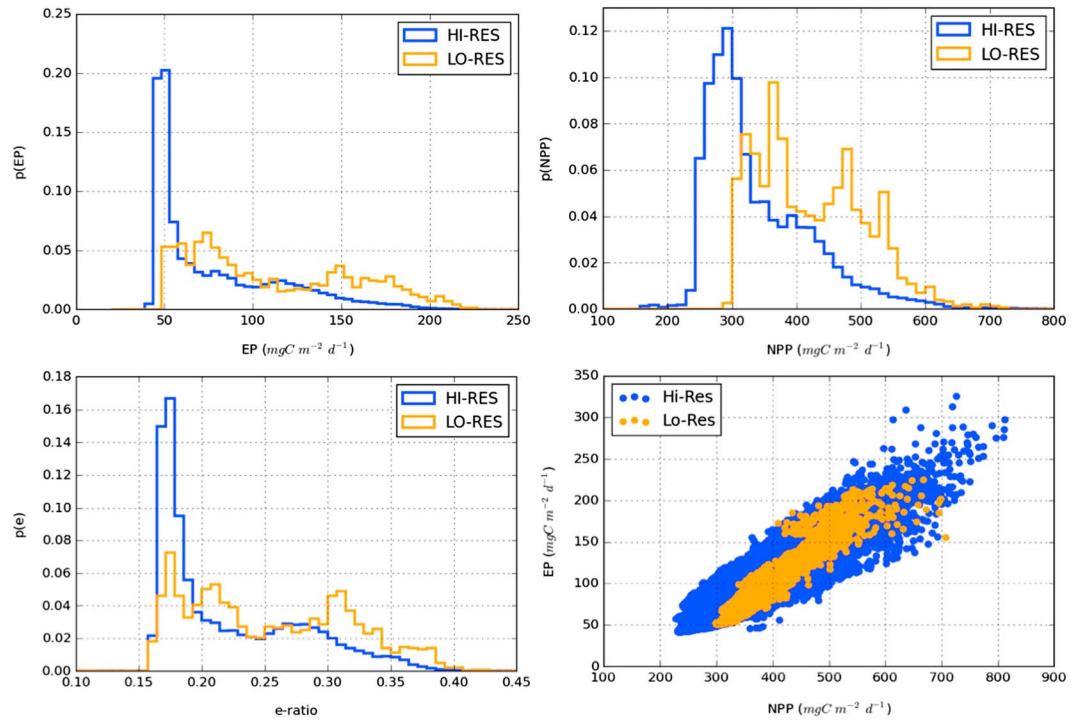
3.3.1.2. South Atlantic

Similar to the North Pacific, the Argentine Basin in the South Atlantic is iron limited (Figure 6); here again, off-shelf transport of iron from shelf sediments is restricted by a coastal jet, in this case the strong Malvinas Current (Figure 11). Energetic waters of the ACC are carried in this current, following the Argentine shelf break, transporting nitrate- and silica-rich but iron-poor waters northward. The Malvinas Current meets the southward flowing Brazil Current, which brings nitrogen-poor subtropical waters from the north. The meeting of the two jets results in an energetic mesoscale turbulence field, reaching across the Atlantic, with an associated seasonal bloom (Figure 7), delivering a large fraction of the region's export flux (Figure 1), and associated with a high export ratio (Figures 1 and 4). The circulation in this region is better represented relative to observations in the HI-RES model simulation than in LO-RES (cf. Combes & Matano, 2014).

Improved resolution of the coastal jet, as well as restriction of productivity into a smaller spatial area within the turbulent region off the shelf, together limit productivity and export in the HI-RES simulation. A larger horizontal supply of sedimentary iron in LO-RES creates a seasonal bloom that is more widespread in space, extends farther from the coast, and in this case persists more than a month longer than in the HI-RES model (Movies S3–S4_LR, EP_global_HR). This more intense, broader, and longer bloom results in greater regional NPP, EP, and again a corresponding higher e-ratio in the LO-RES simulation than in HI-RES (Figures 1 and 3–5), so that integrated EP in the East Southern Ocean is 9.4% greater (Table 1). Here there is also a difference in the spatial location of production through a shift in the location of the Malvinas-Brazil confluence with changing resolution, a phenomena seen for western boundary currents (Small et al., 2014).

As in the North Pacific, resolution of the mesoscale circulation in the Argentine Basin changes the spatial structure of the bloom to a large degree (Figure 12). With mesoscale resolution, the highly energetic, turbulent flow drives a constant interaction between eddies of many sizes, as well as transitory jets and filaments, and these features are typically not coherent for more than a few weeks. In HI-RES, production is highly modulated by this intense mesoscale flow, often constrained into patchy streams between and around vortices

Figure 10. Probability distributions for the North Pacific of annual mean export production (EP), net primary productivity (NPP), e-ratio, and a scatter plot of EP versus NPP for the HI-RES (blue) and LO-RES (orange). Distributions are taken over 45–60°N and 140–220°E, using the native simulation resolution.

(Figure 12, Movie S2). In HI-RES, export is sometimes high around vortices, sometimes within, sometimes associated with transient filaments, but largely chaotic and incoherent. The bloom is filamentary to an extent that high spatial variance is retained in the annual means of biomass, EP, NPP, and the e-ratio for the region (Figures 11, 1 and 3–5), as also indicated by the broader range of values in joint distributions of NPP
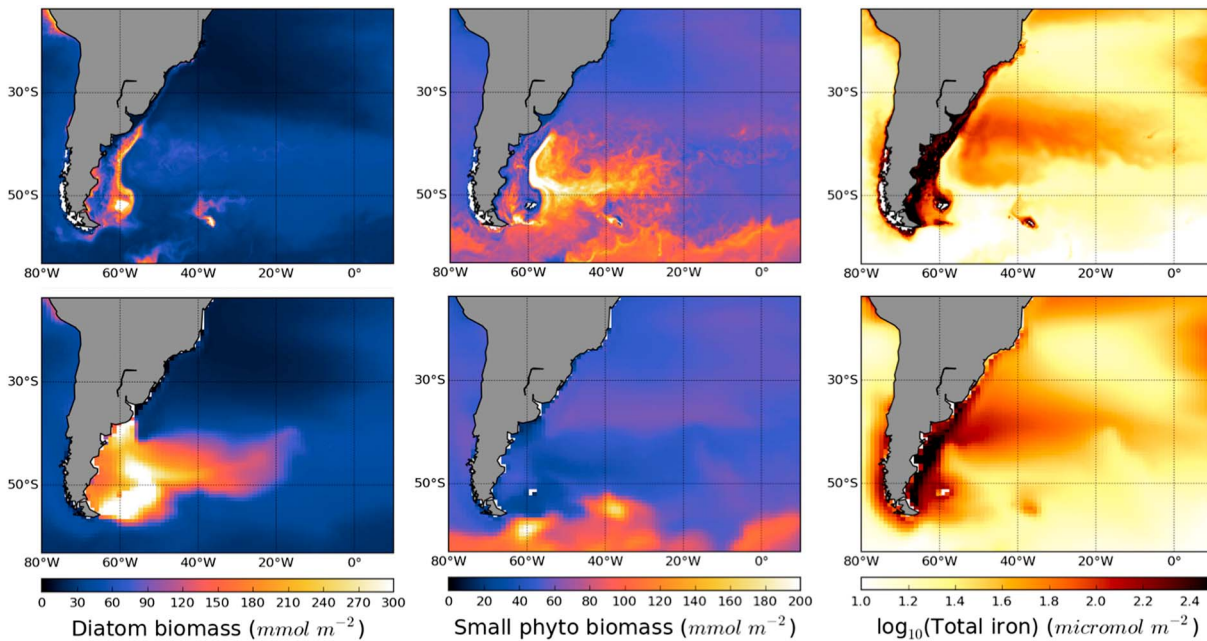

Figure 11. Annual mean biomass and total iron in the South Atlantic, integrated over the top 100 m. Top is HI-RES, bottom is LO-RES, left is diatom carbon biomass, middle is small phytoplankton carbon biomass, and right is total iron. Zonation of phytoplankton types occurs in the HI-RES simulation, resulting in a change in community structure off the Patagonian shelf.
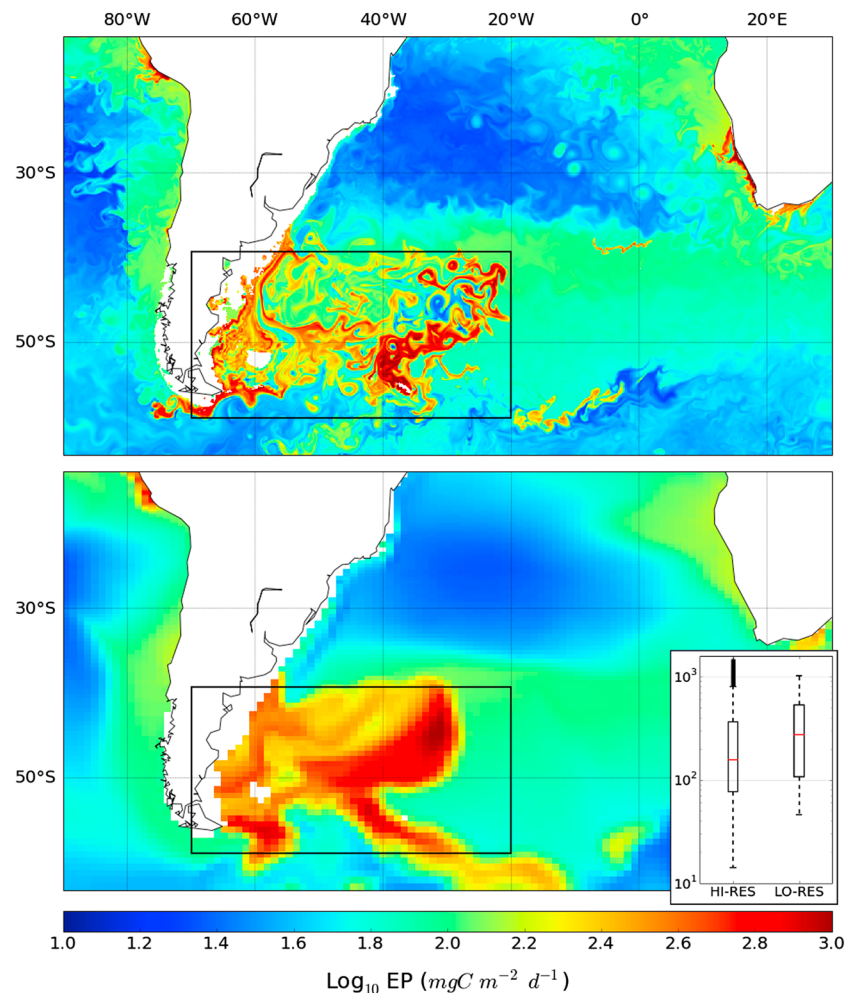
Figure 12. Export production on 25 January in the HI-RES (top) and LO-RES (bottom) simulations, shown in log scale. Spatial variance is greater in HI-RES, such that the range of values is broader (inset, statistics taken over boxed regions), and resulting in a reduction in the median (157 mg C $m^{-2}d^{-1}$ in HI-RES versus 273 in LO-RES), mean (200 versus 284 mg C $m^{-2}d^{-1}$), and spatially integrated (0.44 versus 0.64 Pg C yr^{-1}) values of export production (EP) on this day.

and EP (Figure 13). The highly energetic, variable nature of the flow in this region, combined with the short season of production, drives a high standard deviation in the local annual mean export ratio (Figure 7), due to the mesoscale-driven internal variability. In contrast, the LO-RES simulation features a wide, coherent front of production and export that propagates uniformly eastward (Figure 12, Movie S3).

Unlike the chaotic, incoherent flow of the Argentine Basin, votices to the northeast (the Agulhas rings) retain their coherence for months to years, propagating northwest from South Africa to Brazil through the quiescent subtropical gyre (Froyland et al., 2015; Wang et al., 2015). In the HI-RES model, these long-lived vortices have clear spatial coherence in their biological response relative to the surrounding waters (Figure 12, Movie S2). The biogeochemical environment within the vortices changes over time, apparently depending on both the waters entrained in their interiors upon formation, as well as the interaction of the vortices with synoptic variability in the atmospheric forcing. In the modeled Agulhas rings, like in the North Pacific, production and export are sometimes greatest within vortices, sometimes on the edges of vortices, and sometimes outside, changing over time for an individual vortex. In sum, the persistently coherent Agulhas rings have only a limited contribution to carbon production and export in the region, which is overwhelmingly dominated by the turbulent, largely incoherent, production to the southwest (Figure 12).

In contrast to the North Pacific, reduction in iron concentration in the Argentine Basin is sufficient to drive a shift from a bloom dominated by diatoms in the low-resolution model to a bloom dominated by small
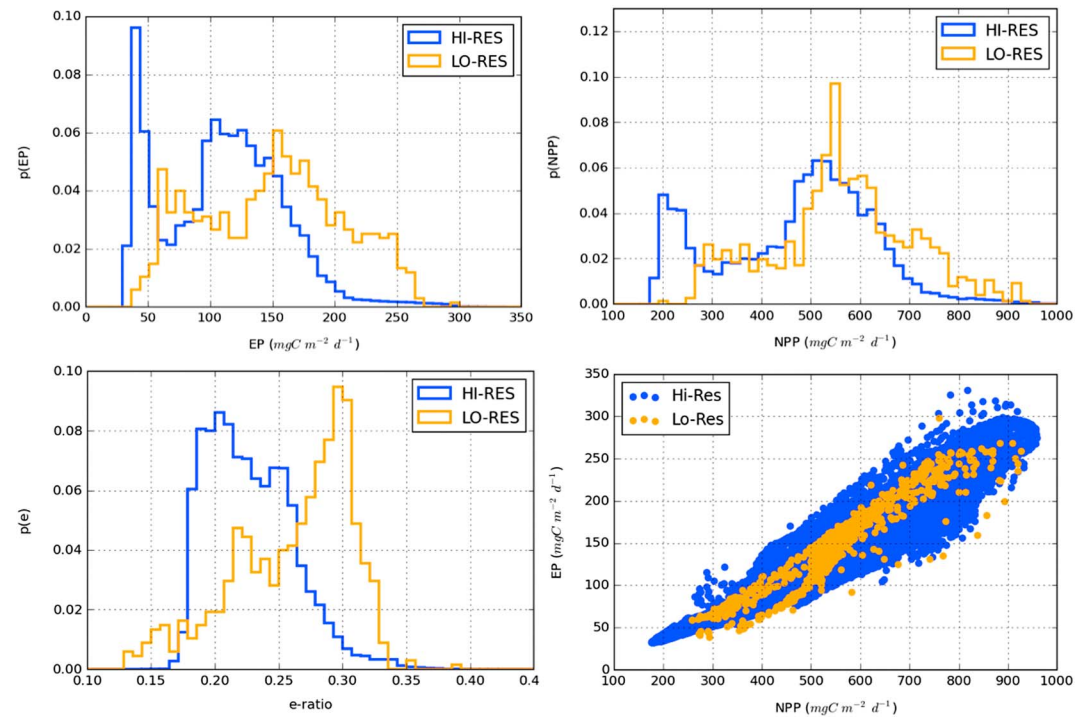
Figure 13. As in Figure 10 but for the South Atlantic. Distributions are taken over 40–57°S and 40–70°W. EP = export production; NPP = net primary productivity.

phytoplankton with higher resolution (Figure 11). In the CESM-BEC model parameter set used here (Lima et al., 2014), diatoms grow faster than small phytoplankton only in high nutrient, lower light conditions (Figure S3), in part due to their modeled greater ability for photoadaptation (Geider et al., 1998). Thus, the light and nutrient distributions at the beginning of the growing season affect the dominance of one plankton type over another, especially at high latitudes where light is more limiting. In the HI-RES simulation, iron limitation is sufficient off the shelf to cause small phytoplankton to dominate, despite the high nitrate availability. Restriction of iron transport by the Malvinas in HI-RES causes the bloom to be spatially zoned, so that diatoms are largely confined to inside this coastal jet where iron concentration is higher, while small phytoplankton dominate the off-shelf area, except for a small region of natural iron fertilization around South Georgia Island.

Also, in contrast to the North Pacific, where the e-ratio probability distributions are similar in shape (i.e., same mode) but enhanced for high values in the LO-RES simulation (Figure 10), export ratio distributions for the South Atlantic are distinctly different between the two simulations (Figure 13). The mode value of the export ratio decreases from 0.3 in the LO-RES simulation to 0.2 in the HI-RES simulation, consistent with small phytoplankton leading to lower export efficiency than diatoms in the BEC model. Interestingly, in regions of substantial calcite production, POC derived from small phytoplankton has a higher transfer efficiency in BEC due to mineral ballasting (Lima et al., 2014), so that in HI-RES the export to 2,000 m is greater for the South Atlantic (not shown), due to the shift in community structure, even though the EP at 100 m is substantially smaller. This result indicates how resolving mesoscale circulation can affect basin-scale biogeochemical processes.

3.3.2. Vertical Changes in Nutrient Delivery

Higher horizontal model resolution can increase vertical transport of nutrients through a number of mechanisms. Higher horizontal resolution increases the coastal upwelling flux (Small et al., 2014, 2015), bringing more nutrients to the surface and thus increasing local productivity, for example, in Benguela upwelling region off South Africa (Figure 12). Increasing horizontal resolution also leads to differences in air-sea interactions, especially near better resolved fronts, affecting vertical mixed layer dynamics and thus productivity and export (Koszalka et al., 2009; Omand et al., 2015; Whitt et al., 2016).

Vertical mixing has competing effects on productivity and export. Vertical mixing can bring nutrients to the surface, increasing productivity; deep mixed layers inhibit productivity by limiting light for photosynthesis,
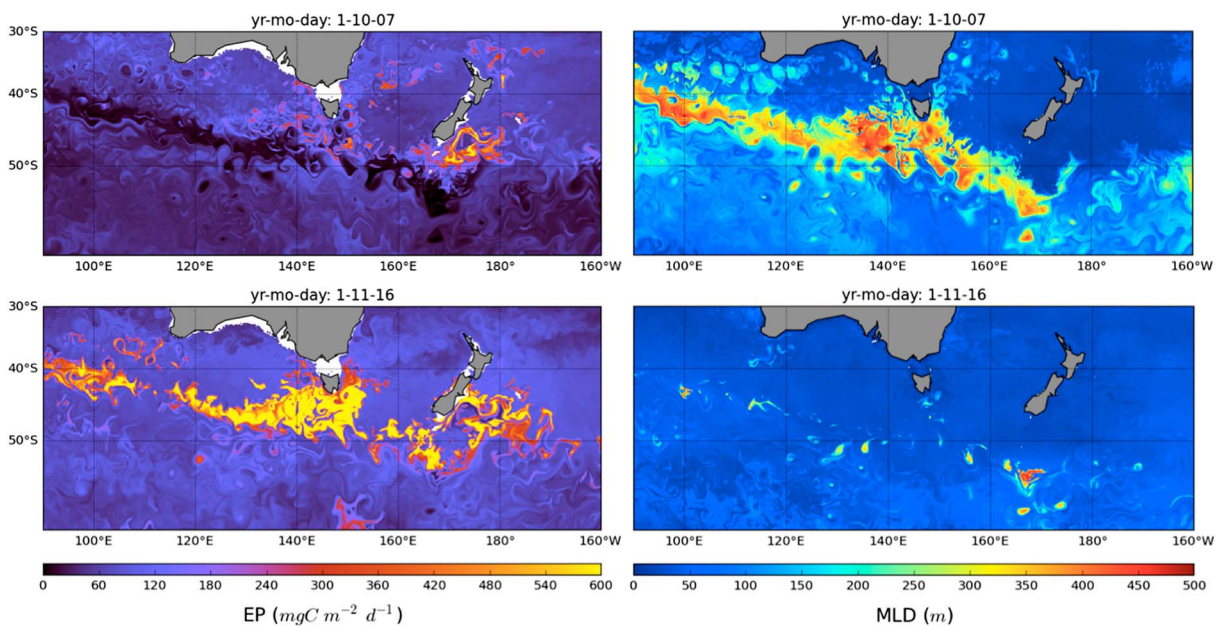
Figure 14. Export production (EP, left) and average mixed layer depth (MLD, right) in the Southern Ocean south of Australia for two 5 day mean model output snapshots, before (top) and after (bottom) deep mixed layers restratify in late spring.

so that extended deep mixing will reduce net productivity and export. Vertical mixing can also relieve grazing pressure by diluting prey, making predation less efficient (Rohr et al., 2017); additionally, the model includes a reduced grazing loss at very low prey biomass levels (Moore et al., 2001, 2004). When deep mixed layers restratify and shoal, large blooms can occur, as phytoplankton respond faster than zooplankton to the newly favorable light and nutrient conditions, initially growing without strong grazing control. Here we highlight one region where this last effect is especially important for locally enhancing productivity and export: the Subantarctic.

3.3.2.1. Sub-Antarctic

Together, the Indian and Pacific sectors of the Southern Ocean generate over 1 Pg C yr^{-1} in carbon export flux (West Southern Ocean basin in Table 1), representing about 20% of the global total. While basin integrated EP in this region is similar in the two simulations, the spatial distribution differs substantially (Figure 1). Relative to the LO-RES simulation, productivity and export in HI-RES are more focused in a narrow zonal swath in the Subantarctic along the northern flank of the ACC and reduced to the north and south of this (Figures 1 and 3). This change in location of NPP and EP is also associated with a change in the e-ratio, with regions of higher productivity in the HI-RES simulation having a higher e-ratio, and vice versa. The shift in the regions of high productivity, export flux, and e-ratio is correlated with differences in MLD between the two simulations (Figure 5). Deep winter mixed layers exert a strong control on the location of the spring bloom across the subantarctic Pacific and Indian sectors, consistent with observations (Tagliabue et al., 2014).

In the Subantarctic, deep mixed layers (>250 m) persist throughout the winter and into the spring (Dong et al., 2008; Kara et al., 2003), driven by interactions between weakly stable stratification and strong winds (de Boyer Montégut et al., 2004; Rintoul & England, 2002). Replicating deep frontal mixed layers in ESMs is problematic due to the small lateral scale of these features and the coarse resolution of the models (Sallée et al., 2013). The LO-RES simulation produces subantarctic mixed layers that are too shallow and displaced from the observed maximum locations (Figures 5 and S2) (de Boyer Montégut et al., 2004; Kara et al., 2003). In the HI-RES simulation, subantarctic deep mixed layers are enhanced, narrowed, and in the appropriate regions, though still too shallow and less persistent in time, beginning later and restratifying earlier in the season than observed (June–October instead of May–November, Kara et al., 2003). The timing, horizontal and vertical extent, and seasonality of these deep mixed layers affect annual mean regional productivity and export.

The Southern Ocean has low iron concentrations (Figure 6) but elevated concentrations of all other limiting nutrients. Persistent, deep winter mixing brings iron to the surface, resulting in a large phytoplankton bloom
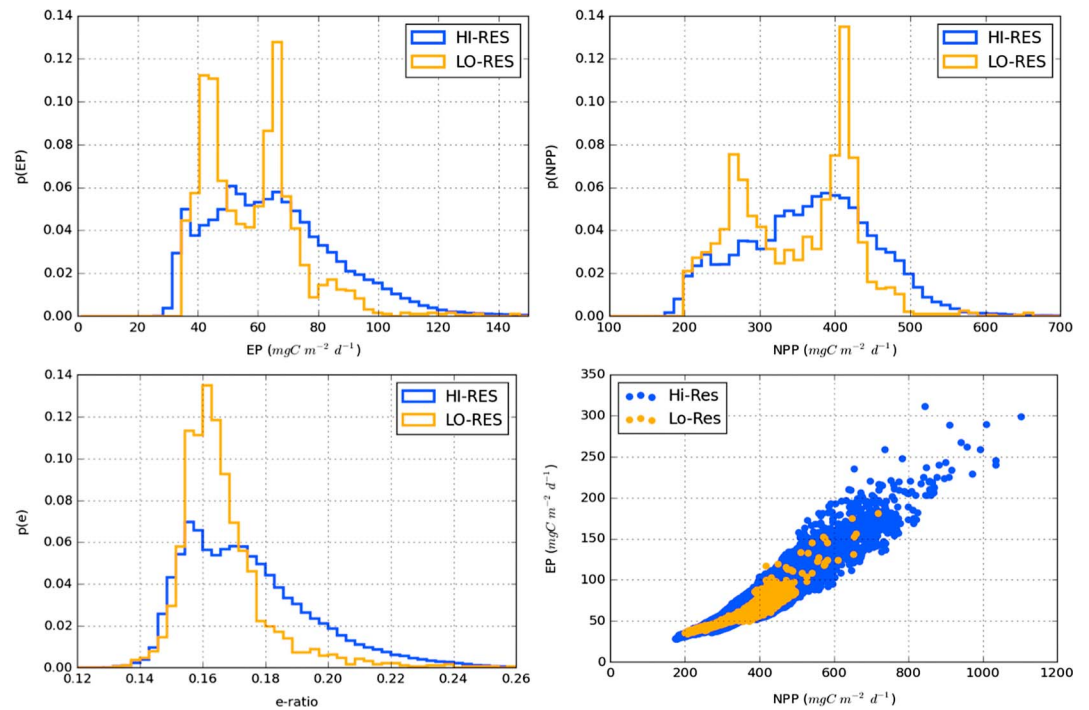
Figure 15. As in Figure 10 but for the Subantarctic near Australia. Distributions are taken over 40–55°S and 120–200°E. EP = export production; NPP = net primary productivity.

after restratification (Tagliabue et al., 2014). In our model, the iron flux is not sufficient to promote diatom growth over small phytoplankton (Figure S3), so that small phytoplankton dominate the bloom, with only a small diatom response at the beginning of the season when iron is highest. Zooplankton dilution during deep mixing aids in the initial bloom growth, as it takes about a week longer for zooplankton to respond to the increased prey field than it takes for the phytoplankton to respond to favorable growing conditions (not shown).

Snapshots of the MLD and EP illustrate the spatiotemporal control mesoscale features have on both vertical mixing and export (Figure 14). In October deep mixing occurs over a wide, meandering zonal swath, and within the nearby vortices to the north and south. This swath corresponds to a region of very low EP during deep mixing, as all plankton are diluted and effectively light limited. By mid-November the ocean is largely restratified and EP is large where mixed layers were deep, strongly modulated in space by the mesoscale circulation. The majority of the large export signal in the Pacific and Indian Subantarctic occurs over just a 2 month period in the HI-RES model (Figure 7), with local enhancement before and after the restratification-driven spring bloom due to sediment-derived iron horizontal transport around the New Zealand and Kerguelen Plateaus (Movie S4).

Regions of greater productivity and export in the subantarctic Pacific are also associated with higher values of the mean e-ratio (Figures 1 and 5). This is the result of the same spatial effect as seen in the North Pacific: enhancement of the spatial extent of the bloom, this time for the HI-RES simulation relative to the LO-RES simulation, driven by vertical rather than horizontal processes. Enhanced iron supply by deeper and more spatially extensive vertical mixing in the HI-RES simulation drives a more expansive and stronger bloom, elevating the tails of the EP, NPP, and e-ratio distributions (Figure 15), shifting the means to higher values.

3.3.2.2. Tropics and Western Boundary Extensions

Vertical nitrate fluxes are greater in the HI-RES model across the tropics and in western boundary extension regions (not shown), associated with increases in NPP and EP (Figures 1 and 3) for nitrate limited areas (Figure 6). These regions of increased productivity are also associated with greater mean MLDs (Figure 5), suggesting that eddy-mediated increases in vertical mixing are driving changes in productivity, as has been found in previous mesoscale resolving modeling studies (Mahadevan, 2016; McGillicuddy, 2016). Due to greater seasonality at higher latitudes (Figure 7), there is a nonlinear relationship in how much enhanced vertical mixing
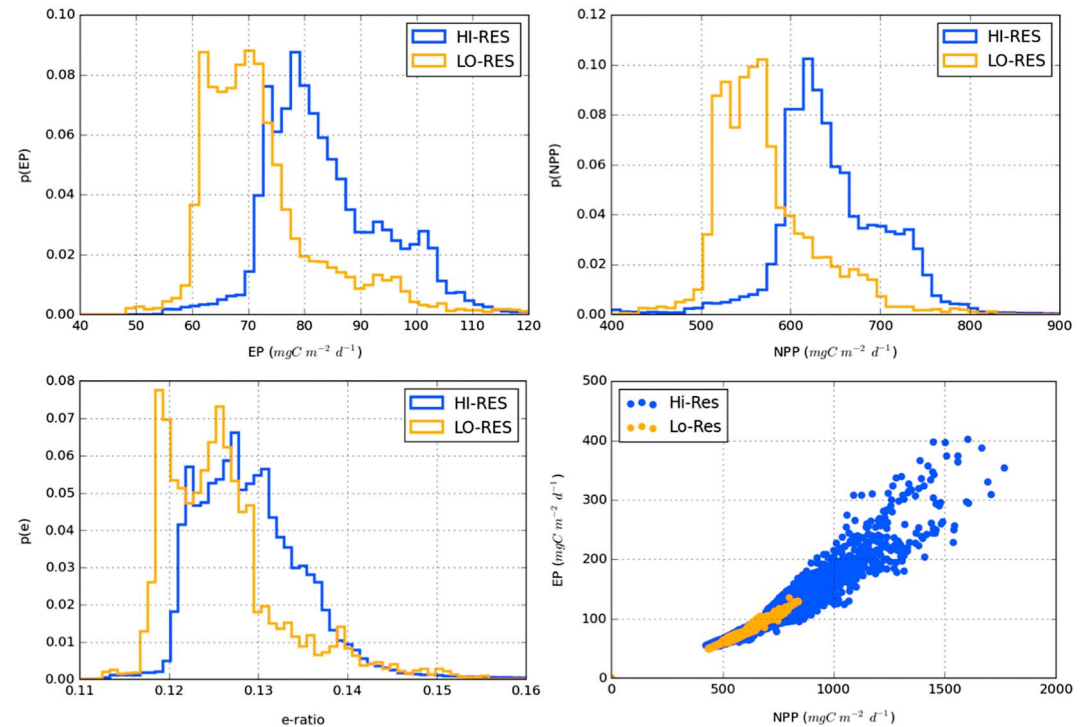
Figure 16. As in Figure 10 but for the Indian ocean. Distributions are taken over −15–25°N and 40–100°E. EP = export production; NPP = net primary productivity.

may in turn enhance production and export. For example, in the Kuroshio and Gulf Stream extensions, intense vertical mixing occurs largely in winter, when production is temperature and light limited, so that nutrient injections are poorly utilized. A smaller amount of vertical mixing enhancement in the tropics, spread out over a longer period in which growth conditions are consistently favorable, results in a corresponding greater enhancement of production and export.

Enhanced productivity and export occur across the tropics in the HI-RES simulation where nitrate is the limiting factor (Figures 1, 3 and 6). The exception is the eastern Pacific, where the iron limitation is not alleviated by the enhanced vertical mixing, as there is little iron at depth (not shown). The result is a net null effect of changing resolution on carbon export in the tropical Pacific when integrated over the basin (Table 1), as increases in production in the west are balanced by decreases in production in the east. In the eastern Pacific, iron transport from the coast and Galapagos Islands is again limited by the reduction in horizontal transport at higher resolution.

Changes in NPP and EP in the tropics do not correlate with a corresponding change in the export ratio to the extent seen in other regions (Figure 4). In contrast to the North Pacific and South Atlantic, where production was divided into patchy, blooming regions of high productivity and export in a background flow of low productivity and export, production and export across the tropics extends over the entire year with little spatial variance (Figure 7, Movie S4). Changes in vertical nutrient delivery in the tropics are less intense in magnitude and more distributed in space and time, so less modulated by the mesoscale circulation. This is associated with differences in EP and NPP distributions that shift the entire distribution to higher values (Figure 16; Indian NPP median = 636 mg C $m^{-2}d^{-1}$ in HI-RES versus 561 LOW-RES; EP median = 82 mg C $m^{-2}d^{-1}$ in HI-RES versus 70 in LOW-RES), rather than just enhancement of the tails of the distributions, as was found in the Subantarctic (Figure 15), resulting in only a small change in the mean e-ratio.

4. Summary and Discussion

We compared oceanic particulate carbon export in two simulations of the CESM-BEC ocean component, one at the standard 1° horizontal resolution (LO-RES) and one at eddy-resolving 0.1° resolution (HI-RES), both forced with the same data sets. Over 40% of global EP occurs in regions of iron limitation in the model,

indicating the strong control of iron on carbon fluxes. While the difference in globally integrated EP between the two simulations is small (<2%), basin-scale differences are over ±10% and local differences can be upward of ±50%. The largest percent differences are in regions of high productivity and export: the North Pacific, Argentine Basin, Subantarctic, and across the tropics where nitrate is limiting. These differences can be attributed to different representation of horizontal and vertical transport with mesoscale resolution, both of which affect nutrient delivery.

Mesoscale dynamics impacts patterns of productivity and export by modulating the horizontal transport of limiting nutrients. In the North Pacific and Argentine Basin, off-shelf total iron inventories are drastically reduced (over 50 times less) in the HI-RES relative to the LO-RES simulation. This difference is due to resolution of the mesoscale flow in the HI-RES simulation, which affects off-shelf delivery of sediment-derived iron by two mechanisms: stronger coastal jets in the HI-RES simulation act as transport barriers, blocking off-shelf transport; resolution of mesoscale turbulence in HI-RES limits the spatial extent of the iron delivery that does make it off the shelf, reducing the bloom to a smaller area. In both of these regions, EP is equally reduced by a decrease in NPP and the fraction of NPP that is exported (e-ratio). The reduction of iron in the Argentine Basin is sufficient to shift community composition from diatoms to small phytoplankton, further reducing the regional e-ratio, as small phytoplankton carbon is exported less efficiently in the BEC model. The difference in continental shelf jet structure between the two simulations represents a difference in mean flow that cannot be well represented as a diffusive mixing process. In short, the subgrid-scale parameterizations used in non-eddy-resolving ESMs overdiffuse shelf-derived iron inputs at the ocean surface, resulting in higher regional production, affecting basin-scale biogeochemical cycles. Use of nonisotropic eddy parameterizations (Smith & Gent, 2004) may help to ameliorate this effect and should be tested for their effect on biogeochemical tracers.

Vertical delivery of limiting nutrients also impacts export. In the Subantarctic, regions of high productivity are driven by deep winter mixing bringing limiting iron to the euphotic zone. An intense seasonal bloom occurs when these areas restratify in the spring. The result is strong positive spatial correlations in differences between the two simulations across the Indian and Pacific sectors of the Southern Ocean for a number of variables: the mean annual MLD, NPP, EP, and the e-ratio. In the HI-RES simulation, regions of deep mixing are shifted and narrowed in space and enhanced in depth by up to 50%, yielding better correspondence with observations for both location and intensity. The difference in winter mixing results in more intense, spatially restricted productivity and export in the HI-RES simulation. Here the differences in EP are again driven equally by changes in NPP and e-ratio. Across the tropics where iron is not the limiting nutrient, such as the Indian and Atlantic Oceans, EP is higher locally by up to 50% in the HI-RES simulation. This is almost entirely due to changes in NPP, as changes in e-ratio are small. The tropics have a higher eddy-driven vertical nitrate flux, consistent with previous modeling studies (e.g., Clayton et al., 2017; Lévy, Iovino, et al., 2012). We conclude that enhanced vertical nutrient supply in the HI-RES simulation, spread over the long tropical growing season, drives higher annual mean production and export.

Globally, seasonality of EP, combined with the internal variability of the eddy-resolving model simulation, affects interannual variability of EP and e-ratio. The North Pacific, Argentine Basin, and Subantarctic are all characterized by short growing seasons. This seasonality, combined with locally strong mesoscale turbulence, results in locally high variability in the annual mean e-ratio in HI-RES. In these regions production and export are sometimes high within coherent vortices, sometimes high around coherent vortices, but mostly spatially incoherent due to the nature of chaotic turbulent flow. Thus, in regions of high seasonality, where all of the EP occurs over just a few months, chaotic flow leads to a high degree of variability in the annual mean e-ratio (Figure 7), a manifestation of the internal variability of the mesoscale ocean. This makes observational campaigns in these regions of intense, brief EP especially prone to sampling bias, which is problematic in that they are also the regions of greatest EP. In these turbulent regions, submesoscale biophysical impacts on production and export, not resolved here, could also be significant (Mahadevan, 2016). Careful consideration of the effects of EP spatiotemporal patchiness on observational estimates of net regional biogeochemical cycles is needed (e.g., Estapa et al., 2015; Resplandy et al., 2012), and high-resolution modeling efforts are valuable for informing observational campaign design, as well as validating model parameterizations.

The 5 year length of the HI-RES simulation is not sufficient to assess long-term changes in the ocean physical biogeochemical mean state due to resolution of mesoscale processes. In particular, we initialized the biogeochemical tracers to observed distributions; thus, the long-term effects of the eddying flow are not fully realized

and cannot be assessed in our experimental framework, though significant changes to the biogeochemical background state are to be expected with longer integration (Lévy, Iovino, et al., 2012). We can asses model biogeochemical drift during the 5 year simulations. Drift in EP was apparent in both integrations, but these drifts were largely consistent between the two model simulations for the basins of greatest change. EP notably decreases in the Indian and tropical Atlantic basins, resulting in ~5% reduction in the local annual mean EP from year 1 to year 5 in both simulations, opposite in sign and much smaller in magnitude than the difference between the two simulations. This reduction in EP is associated with decreases in NPP and all nutrients in the top 100 m, indicating some lack of fidelity between both model simulations and the initial biogeochemical conditions. Over most of the ocean, the difference in the EP annual means over the 5 years of the HI-RES simulation is very small or locally patchy, attributable to internal variability in short season, chaotic flow regions where spatial variance of NPP, EP, and e-ratio are all high (Figure 7). Thus, we cannot ascribe a significant difference between the two simulations' biogeochemical background states over the 5 year integration time that is clearly due to mesoscale resolution. This is an important topic for future research as computational resources become available.

We have not focused on trophic controls on export and export efficiency. We found that changes in primary production, driven by changes in physical circulation and nutrient delivery, were the primary control in enhancing or diminishing export moving from low to high resolution. This result may be dependent on the biogeochemical model used. It should be noted that routing of carbon through the various plankton components is highly variable between different ESMs and exerts a strong control on their biogeochemical response under climate change (Laufkötter et al., 2015, 2016). Observational campaigns are proposed to assess trophic controls on export efficiency (Siegel et al., 2016). These observations should be compared with the results here to assess how well BEC is representing the food web pathways and other processes controlling export patterns.

Our results highlight how potentially sensitive global ESMs are to parameterizations of iron delivery. Great uncertainty exists in how to best represent iron inputs and cycling in ESMs (Dale et al., 2015; Tagliabue et al., 2016). Results here further implicate the role of mesoscale circulation in constraining the horizontal delivery of coastal iron, as well as vertical delivery of subsurface open-ocean iron, which we have found are controlling the spatiotemporal structure of productivity and export in iron-limited regions. Our results suggest that the coarse-resolution CESM overestimates the flux of continental shelf-derived dissolved iron to the open ocean in key high-export regions due to two mechanisms: strong coastal jets acting as transport boundaries and turbulence-driven spatial restriction of the resulting bloom. Both of these processes warrant attention for better parameterization in coarse-resolution climate models. Alternately, the representation of iron sediment inputs may need to depend on model resolution, compensating for the reduction in transport at higher resolution and/or topographic resolution.

Eddy parameterizations developed for active and passive tracers in ESMs may not be as effective for reactive tracers (which react to strong gradients in the flow but do not affect the dynamics), such as biogeochemical variables. This indicates that some effort toward improvement is warranted, especially in regions of strong eddy activity and high seasonality. Theoretical modeling work has demonstrated that effective eddy diffusivity is smaller for reactive tracers than for passive tracers and that this effect can elevate productivity in lower resolution, consistent with this study (Pasquero, 2005). The details of this effect depends on both the reaction time scale of the tracer and the advective time scale of the circulation, which both vary depending on the tracer in question and how energetic the regional dynamics are. These results indicate that there may be a better way to parameterize eddies for reactive tracers based on the local flow dynamics and the type of tracer.

Are global high-resolution modeling efforts worth the computational cost? Here global integrals of export and primary production differ by less than 2% when the mesoscale is resolved, while the computational cost scales geometrically with increasing resolution. However, this fidelity between the model resolutions arises due to regional compensating differences, and differences could be larger if parameterizations were adjusted. More importantly, the large local and regional differences between the mesoscale and standard resolution simulations suggest that great caution is needed when comparing ESMs with in situ observations, which are inherently local. Further, observations are strongly affected by mesoscale ocean variability, which we have shown is largest in many regions of greatest production and export, and these are the exact regions where the HI-RES model shows the greatest difference from the standard resolution ESM, underscoring the pitfalls

of ESM validation for primary and EP. Much work is needed to tackle the biogeochemical validation challenge in these regions, in particular, and both regional and global mesoscale resolving, and indeed submesoscale resolving (Mahadevan, 2016), model simulations are needed to make progress, both in informing the design of sampling campaigns and in continuing to assess what we are missing at coarse resolution.

References

Abraham, E. R. (1998). The generation of plankton patchiness by turbulent stirring. *Nature*, 391(6667), 577–580. https://doi.org/10.1038/35361

Abraham, E. R., Law, C. S., Boyd, P. W., Lavender, S. J., Maldonado, M. T., & Bowie, A. R. (2000). Importance of stirring in the development of an iron-fertilized phytoplankton bloom. *Nature*, 407(6805), 727–730. https://doi.org/10.1038/35037555

Anderson, L. A., McGillicuddy, D. J., Maltrud, M. E., Lima, I. D., & Doney, S. C. (2011). Impact of eddy-wind interaction on eddy demographics and phytoplankton community structure in a model of the North Atlantic Ocean. *Dynamics of Atmospheres and Oceans*, 52, 80–94. https://doi.org/10.1016/j.dynatmoce.2011.01.003

Armstrong, R., Lee, C., Hedges, J., Honjo, S., & Wakeham, S. (2002). A new, mechanistic model for organic carbon fluxes in the ocean based on the quantitative association of POC with ballast minerals. *Deep-Sea Research*, 49(1–3), 219–236. https://doi.org/10.1016/S0967-0645(01)00101-1

Berger, W. H., & Wefer, G. (1990). Export production: Seasonality and intermittency, and paleoceanographic implications. *Global and Planetary Change*, 3(3), 245–254. https://doi.org/10.1016/0921-8181(90)90020-D

Bracco, A., Clayton, S., & Pasquero, C. (2009). Horizontal advection, diffusion, and plankton spectra at the sea surface. *Journal of Geophysical Research*, 114, C02001. https://doi.org/10.1029/2007JC004671

Buesseler, K. O., & Boyd, P. W. (2009). Shedding light on processes that control particle export and flux attenuation in the twilight zone of the open ocean. *Limnology and Oceanography*, 54(4), 1210–1232. https://doi.org/10.4319/lo.2009.54.4.1210

Burd, A. B., & Jackson, G. A. (2009). Particle aggregation. *Annual Review of Marine Science*, 1(1), 65–90. https://doi.org/10.1146/annurev.marine.010908.163904

Carlson, C. A., Ducklow, H. W., & Michaels, A. F. (1994). Annual flux of dissolved organic carbon from the euphotic zone in the northwestern Sargasso Sea. *Nature*, 371(6496), 405–408. https://doi.org/10.1038/371405a0

Clayton, S., Dutkiewicz, S., Jahn, O., & Follows, M. J. (2013). Dispersal, eddies, and the diversity of marine phytoplankton. *Limnology and Oceanography: Fluids and Environments*, 3(1), 182–197. https://doi.org/10.1215/21573689-2373515

Clayton, S., Dutkiewicz, S., Jahn, O., Hill, C., Heimbach, P., & Follows, M. J. (2017). Biogeochemical versus ecological consequences of modeled ocean physics. *Biogeosciences; Katlenburg-Lindau*, 14(11), 2877–2889. https://doi.org/10.5194/bg-14-2877-2017

Combes, V., & Matano, R. P. (2014). A two-way nested simulation of the oceanic circulation in the Southwestern Atlantic. *Journal of Geophysical Research: Oceans*, 119, 731–756. https://doi.org/10.1002/2013JC009498

Combes, V., Di Lorenzo, E., & Curchitser, E. (2009). Interannual and decadal variations in cross-shelf transport in the Gulf of Alaska. *Journal of Physical Oceanography*, 39(4), 1050–1059. https://doi.org/10.1175/2008JPO4014.1

Dale, A. W., Nickelsen, L., Scholz, F., Hensen, C., Oschlies, A., & Wallmann, K. (2015). A revised global estimate of dissolved iron fluxes from marine sediments. *Global Biogeochemical Cycles*, 29, 691–707. https://doi.org/10.1002/2014GB005017

Danabasoglu, G., McWilliams, J. C., & Gent, P. R. (1994). The role of mesoscale tracer transports in the global ocean circulation. *Science*, 264(5162), 1123–1126. https://doi.org/10.1126/science.264.5162.1123

Danabasoglu, G., Yeager, S. G., Bailey, D., Behrens, E., Bentsen, M., Bi, D., et al. (2014). North atlantic simulations in Coordinated Ocean-ice Reference Experiments Phase II (CORE-II). Part I: Mean states. *Ocean Modelling*, 73, 76–107. https://doi.org/10.1016/j.ocemod.2013.10.005

de Boyer Montégut, C., Madec, G., Fischer, A. S., Lazar, A., & Iudicone, D. (2004). Mixed layer depth over the global ocean: An examination of profile data and a profile-based climatology. *Journal of Geophysical Research*, 109, C12003. https://doi.org/10.1029/2004JC002378

de Lavergne, C., Palter, J. B., Galbraith, E. D., Bernardello, R., & Marinov, I. (2014). Cessation of deep convection in the open Southern Ocean under anthropogenic climate change. *Nature Climate Change*, 4(4), 278–282. https://doi.org/10.1038/nclimate2132

Delworth, T. L., Rosati, A., Anderson, W., Adcroft, A. J., Balaji, V., Benson, R., et al. (2011). Simulated climate and climate change in the GFDL CM2.5 high-resolution coupled climate model. *Journal of Climate*, 25(8), 2755–2781. https://doi.org/10.1175/JCLI-D-11-00316.1

DeVries, T., & Weber, T. (2017). The export and fate of organic matter in the ocean: New constraints from combining satellite and oceanographic tracer observations. *Global Biogeochemical Cycles*, 31, 535–555. https://doi.org/10.1002/2016GB005551

Doney, S. C., & Ducklow, H. W. (2006). A decade of synthesis and modeling in the US Joint Global Ocean Flux Study. *Deep Sea Research Part II: Topical Studies in Oceanography*, 53(5–7), 451–458. https://doi.org/10.1016/j.dsr2.2006.01.019

Doney, S. C., Lima, I., Moore, J. K., Lindsay, K., Behrenfeld, M. J., Westberry, T. K., et al. (2009). Skill metrics for confronting global upper ocean ecosystem-biogeochemistry models against field and remote sensing data. *Journal of Marine Systems*, 76(1–2), 95–112. https://doi.org/10.1016/j.jmarsys.2008.05.015

Dong, S., Sprintall, J., Gille, S. T., & Talley, L. (2008). Southern Ocean mixed-layer depth from Argo float profiles. *Journal of Geophysical Research*, 113, C06013. https://doi.org/10.1029/2006JC004051

d'Ovidio, F., Della Penna, A., Trull, T. W., Nencioli, F., Pujol, M.-I., Rio, M.-H., et al. (2015). The biogeochemical structuring role of horizontal stirring: Lagrangian perspectives on iron delivery downstream of the Kerguelen Plateau. *Biogeosciences*, 12(19), 5567–5581. https://doi.org/10.5194/bg-12-5567-2015

Downes, S. M., Farneti, R., Uotila, P., Griffies, S. M., Marsland, S. J., Bailey, D., et al. (2015). An assessment of Southern Ocean water masses and sea ice during 1988–2007 in a suite of interannual CORE-II simulations. *Ocean Modelling*, 94, 67–94. https://doi.org/10.1016/j.ocemod.2015.07.022

Dunne, J. P., Armstrong, R. A., Gnanadesikan, A., & Sarmiento, J. L. (2005). Empirical and mechanistic models for the particle export ratio. *Global Biogeochemical Cycles*, 19, GB4026. https://doi.org/10.1029/2004GB002390

Durski, S. M., Kurapov, A., Zhang, J., & Panteleev, G. G. (2016). Circulation in the Eastern Bering Sea: Inferences from a 2-km-resolution model. *Deep Sea Research Part II: Topical Studies in Oceanography*, 134, 48–64. https://doi.org/10.1016/j.dsr2.2015.02.002

Estapa, M. L., Siegel, D. A., Buesseler, K. O., Stanley, R. H. R., Lomas, M. W., & Nelson, N. B. (2015). Decoupling of net community and export production on submesoscales in the Sargasso Sea. *Global Biogeochemical Cycles*, 29, 1266–1282. https://doi.org/10.1002/2014GB004913

Falkowski, P., Scholes, R. J., Boyle, E., Canadell, J., Canfield, D., Elser, J., et al. (2000). The global carbon cycle: A test of our knowledge of earth as a system. *Science*, 290(5490), 291–296. https://doi.org/10.1126/science.290.5490.291

Ferrari, R., & Wunsch, C. (2009). Ocean circulation kinetic energy: Reservoirs, sources, and sinks. *Annual Review of Fluid Mechanics*, *41*(1), 253–282. https://doi.org/10.1146/annurev.fluid.40.111406.102139

Fiechter, J., & Moore, A. M. (2012). Iron limitation impact on eddy-induced ecosystem variability in the coastal Gulf of Alaska. *Journal of Marine Systems*, *92*(1), 1–15. https://doi.org/10.1016/j.jmarsys.2011.09.012

Flato, G. M. (2011). Earth system models: An overview. *Wiley Interdisciplinary Reviews: Climate Change*, *2*(6), 783–800. https://doi.org/10.1002/wcc.148

Fox-Kemper, B., Danabasoglu, G., Ferrari, R., Griffies, S., Hallberg, R., Holland, M. M., et al. (2010). Parameterization of mixed layer eddies. Part III: Implementation and impact in global ocean climate simulations. *Ocean Modelling*, *39*(1–2), 61–78. https://doi.org/10.1016/j.ocemod.2010.09.002

Froyland, G., Horenkamp, C., Rossi, V., & van Sebille, E. (2015). Studying an Agulhas ring's long-term pathway and decay with finite-time coherent sets. *Chaos: An Interdisciplinary Journal of Nonlinear Science*, *25*(8), 083119. https://doi.org/10.1063/1.4927830

Gaube, P., Chelton, D. B., Samelson, R. M., Schlax, M. G., & O'Neill, L. W. (2014). Satellite observations of mesoscale eddy-induced Ekman pumping. *Journal of Physical Oceanography*, *45*(1), 104–132. https://doi.org/10.1175/JPO-D-14-0032.1

Gaube, P., Chelton, D. B., Strutton, P. G., & Behrenfeld, M. J. (2013). Satellite observations of chlorophyll, phytoplankton biomass, and Ekman pumping in nonlinear mesoscale eddies. *Journal of Geophysical Research: Oceans*, *118*, 6349–6370. https://doi.org/10.1002/2013JC009027

Gaube, P., & McGillicuddy, D. J. Jr (2017). The influence of Gulf Stream eddies and meanders on near-surface chlorophyll. *Deep Sea Research Part I: Oceanographic Research Papers*, *122*, 1–16. https://doi.org/10.1016/j.dsr.2017. 02.006

Gaube, P., McGillicuddy, D. J., Chelton, D. B., Behrenfeld, M. J., & Strutton, P. G. (2014). Regional variations in the influence of mesoscale eddies on near-surface chlorophyll. *Journal of Geophysical Research: Oceans*, *119*, 8195–8220. https://doi.org/10.1002/2014JC010111

Geider, R. J., MacIntyre, H. L., & Kana, T. M. (1998). A dynamic regulatory model of phytoplanktonic acclimation to light, nutrients, and temperature. *Limnology and Oceanography*, *43*(4), 679–694.

Gent, P., & McWilliams, J. (1990). Isopycnal mixing in ocean circulation models. *Journal of Physical Oceanography*, *20*(1), 150–155. https://doi.org/10.1175/1520-0485(2003)033<2341:RSFTAC>2.0.CO;2

Gouretski, V., & Koltermann, K. P. (2004). WOCE global hydrographic climatology. *Berichte des BSH*, *35*, 1–52.

Griffies, S. M., Biastoch, A., Böning, C., Bryan, F., Danabasoglu, G., Chassignet, E. P., et al. (2009). Coordinated Ocean-ice Reference Experiments (COREs). *Ocean Modelling*, *26*(1–2), 1–46. https://doi.org/10.1016/j.ocemod.2008.08.007

Gruber, N., & Doney, S. C. (2009). Ocean biogeochemistry and ecology, Modeling of (2nd ed.). In J. H. Steele (Ed.), *Encyclopedia of ocean sciences (second edition)* (pp. 89–104). Oxford: Academic Press.

Gruber, N., Lachkar, Z., Frenzel, H., Marchesiello, P., Münnich, M., McWilliams, J. C., et al. (2011). Eddy-induced reduction of biological production in eastern boundary upwelling systems. *Nature Geoscience*, *4*(11), 787–792. https://doi.org/10.1038/ngeo1273

Harrison, C. S., & Siegel, D. A. (2014). The tattered curtain hypothesis revised: Coastal jets limit cross-shelf larval transport. *Limnology & Oceanography: Fluids & Environments*, *4*, 50–66.

Harrison, C. S., Siegel, D. A., & Mitarai, S. (2013). Filamentation and eddy-eddy interactions in marine larval accumulation and transport. *Marine Ecology Progress Series*, *472*, 27–44.

Hausmann, U., McGillicuddy, D. J., & Marshall, J. (2017). Observed mesoscale eddy signatures in Southern Ocean surface mixed-layer depth. *Journal of Geophysical Research: Oceans*, *122*, 617–635. https://doi.org/10.1002/2016JC012225

Henson, S. A., Sanders, R., & Madsen, E. (2012). Global patterns in efficiency of particulate organic carbon export and transfer to the deep ocean. *Global Biogeochemical Cycles*, *26*, GB1028. https://doi.org/10.1029/2011GB004099

Henson, S. A., Sanders, R., Madsen, E., Morris, P. J., Le Moigne, F., & Quartly, G. D. (2011). A reduced estimate of the strength of the ocean's biological carbon pump. *Geophysical Research Letters*, *38*, L04606. https://doi.org/10.1029/2011GL046735

Henson, S. A., Yool, A., & Sanders, R. (2015). Variability in efficiency of particulate organic carbon export: A model study. *Global Biogeochemical Cycles*, *29*, 33–45. https://doi.org/10.1002/2014GB004965

Houghton, R. A. (2007). Balancing the global carbon budget. *Annual Review of Earth and Planetary Sciences*, *35*(1), 313–347. https://doi.org/10.1146/annurev.earth.35.031306.140057

Hunke, E., & Lipscomb, W. (2008). CICE: The Los Alamos sea ice model, documentation and software user's manual, version 4.0 (Tech. Rep. LA-CC-06-012). Los Alamos National Laboratory.

Hurrell, J. W., Holland, M. M., Gent, P. R., Ghan, S., Kay, J. E., Kushner, P. J., et al. (2013). The Community Earth System Model: A framework for collaborative research. *Bulletin of the American Meteorological Society*, *94*(9), 1339–1360. https://doi.org/10.1175/BAMS-D-12-00121.1

Johnson, K. W., Miller, L. A., Sutherland, N. E., & Wong, C. S. (2005). Iron transport by mesoscale Haida eddies in the Gulf of Alaska. *Deep Sea Research Part II: Topical Studies in Oceanography*, *52*(7–8), 933–953. https://doi.org/10.1016/j.dsr2.2004.08.017

Johnson, R., Strutton, P. G., Wright, S. W., McMinn, A., & Meiners, K. M. (2013). Three improved satellite chlorophyll algorithms for the Southern Ocean. *Journal of Geophysical Research: Oceans*, *118*, 3694–3703. https://doi.org/10.1002/jgrc.20270

Kara, A. B., Rochford, P. A., & Hurlburt, H. E. (2003). Mixed layer depth variability over the global ocean. *Journal of Geophysical Research*, *108*(C3), 3079. https://doi.org/10.1029/2000JC000736

Koszalka, I., Bracco, A., McWilliams, J. C., & Provenzale, A. (2009). Dynamics of wind-forced coherent anticyclones in the open ocean. *Journal of Geophysical Research*, *114*, C08011. https://doi.org/10.1029/2009JC005388

Large, W. G., Danabasoglu, G., Doney, S. C., & McWilliams, J. C. (1997). Sensitivity to surface forcing and boundary layer mixing in a global ocean model: Annual-mean climatology. *Journal of Physical Oceanography*, *27*(11), 2418–2447. https://doi.org/10.1175/1520-0485(1997)027<2418:STSFAB>2.0.CO;2

Large, W. G., McWilliams, J. C., & Doney, S. C. (1994). Oceanic vertical mixing: A review and a model with a nonlocal boundary layer parameterization. *Reviews of Geophysics*, *32*(4), 363–403. https://doi.org/10.1029/94RG01872

Large, W. G., & Yeager, S. G. (2004). Diurnal to decadal global forcing for ocean and sea-ice models: The data sets and flux climatologies. NCAR Tech. Note NCAR/TN 460+STR. https://doi.org/10.5065/D6KK98Q6

Laufkötter, C., Vogt, M., Gruber, N., Aita-Noguchi, M., Aumont, O., Bopp, L., et al. (2015). Drivers and uncertainties of future global marine primary production in marine ecosystem models. *Biogeosciences*, *12*, 6955–6984. https://doi.org/10.5194/bg-12-6955-2015

Laufkötter, C., Vogt, M., Gruber, N., Aumont, O., Bopp, L., Doney, S. C., et al. (2016). Projected decreases in future marine export production: The role of the carbon flux through the upper ocean ecosystem. *Biogeosciences*, *13*(4), 19,941–19,998.

Letscher, R. T., Moore, J. K., Teng, Y. C., & Primeau, F. (2015). Variable C : N : P stoichiometry of dissolved organic matter cycling in the Community Earth System Model. *Biogeosciences*, *12*(1), 209–221. https://doi.org/10.5194/bg-12-209-2015

Lima, I. D., Lam, P. J., & Doney, S. C. (2014). Dynamics of particulate organic carbon flux in a global ocean model. *Biogeosciences*, *11*(4), 1177–1198. https://doi.org/10.5194/bg-11-1177-2014

Lindsay, K., Bonan, G., Doney, S. C., Hoffman, F., Lawrence, D. M., Long, M. C., et al. (2014). Preindustrial control and 20th century experiments with the Earth System Model CESM1(BGC). *Journal of Climate*, *27*(24), 8981–9005. https://doi.org/10.1175/JCLI-D-12-00565.1

Long, M. C., Deutsch, C. A., & Ito, T. (2016). Finding forced trends in oceanic oxygen. *Global Biogeochemical Cycles*, *30*, 381–397. https://doi.org/10.1002/2015GB005310

Long, M. C., Lindsay, K., Peacock, S., Moore, J. K., & Doney, S. C. (2013). Twentieth-century oceanic carbon uptake and storage in CESM1(BGC). *Journal of Climate*, *26*(18), 6775–6800. https://doi.org/10.1175/JCLI-D-12-00184.1

Lovecchio, E., Gruber, N., Münnich, M., & Lachkar, Z. (2017). On the long-range offshore transport of organic carbon from the Canary Upwelling System to the open North Atlantic. *Biogeosciences*, *14*(13), 3337–3369. https://doi.org/10.5194/bg-14-3337-2017

Lévy, M. (2003). Mesoscale variability of phytoplankton and of new production: Impact of the large-scale nutrient distribution. *Journal of Geophysical Research*, *108*(C11), 3358. https://doi.org/10.1029/2002JC001577

Lévy, M. (2008). The modulation of biological production by oceanic mesoscale turbulence. In *Transport and Mixing in Geophysical Flows, Lecture Notes in Physic* (pp. 219–261). Berlin, Heidelberg: Springer. https://doi.org/10.1007/978-3-540-75215-8_9

Lévy, M., Iovino, D., Resplandy, L., Klein, P., Madec, G., Treguier, A. M., et al. (2012). Large-scale impacts of submesoscale dynamics on phytoplankton: Local and remote effects. *Ocean Modelling*, *43*, 77–93. https://doi.org/10.1016/j.ocemod.2011.12.003

Lévy, M., Klein, P., & Treguier, A.-M. (2001). Impact of sub-mesoscale physics on production and subduction of phytoplankton in an oligotrophic regime. *Journal of Marine Research*, *59*(4), 535–565. https://doi.org/10.1357/002224001762842181

Lévy, M. M., Ferrari, R., Franks, P. J. S., Martin, A. P., & Rivière, P. (2012). Bringing physics to life at the submesoscale. *Geophysical Research Letters*, *39*, L14602. https://doi.org/10.1029/2012GL052756

Mahadevan, A. (2016). The impact of submesoscale physics on primary productivity of plankton. *Annual Review of Marine Science*, *8*(1), 161–184. https://doi.org/10.1146/annurev-marine-010814-015912

Maritorena, S., d'Andon, O. H. F., Mangin, A., & Siegel, D. A. (2010). Merged satellite ocean color data products using a bio-optical model: Characteristics, benefits and issues. *Remote Sensing of Environment*, *114*(8), 1791–1804. https://doi.org/10.1016/j.rse.2010.04.002

Martin, A. P. (2003). Phytoplankton patchiness: The role of lateral stirring and mixing. *Progress in Oceanography*, *57*(2), 125–174. https://doi.org/10.1016/S0079-6611(03)00085-5

McClean, J. L., Bader, D. C., Bryan, F. O., Maltrud, M. E., Dennis, J. M., Mirin, A. A., et al. (2011). A prototype two-decade fully-coupled fine-resolution CCSM simulation. *Ocean Modelling*, *39*(1), 10–30. https://doi.org/10.1016/j.ocemod.2011.02.011

McGillicuddy, D. J. (2014). Do Trichodesmium spp. populations in the North Atlantic export most of the nitrogen they fix? *Global Biogeochemical Cycles*, *28*, 103–114. https://doi.org/10.1002/2013gb004652

McGillicuddy, D. J. (2016). Mechanisms of physical-biological-biogeochemical interaction at the oceanic mesoscale. *Annual Review of Marine Science*, *8*(1), 125–159. https://doi.org/10.1146/annurev-marine-010814-015606

McGillicuddy, D. J., Anderson, L. A., Bates, N. R., Bibby, T., Buesseler, K. O., Carlson, C. A., et al. (2007). Eddy/Wind interactions stimulate extraordinary mid-ocean plankton blooms. *Science*, *316*(5827), 1021–1026. https://doi.org/10.1126/science.1136256

McGillicuddy, D. J., Robinson, A. R., Siegel, D. A., Jannasch, H. W., Johnson, R., Dickey, T. D., et al. (1998). Influence of mesoscale eddies on new production in the Sargasso Sea. *Nature*, *394*(6690), 263–266. https://doi.org/10.1038/28367

Misumi, K., Tsumune, D., Yoshida, Y., Uchimoto, K., Nakamura, T., Nishioka, J., et al. (2011). Mechanisms controlling dissolved iron distribution in the North Pacific: A model study. *Journal of Geophysical Research*, *116*, G03005. https://doi.org/10.1029/2010JG001541

Moore, J. K., & Braucher, O. (2008). Sedimentary and mineral dust sources of dissolved iron to the world ocean. *Biogeosciences*, *5*(3), 631–656. https://doi.org/10.5194/bg-5-631-2008

Moore, J. K., Doney, S. C., Glover, D. M., & Fung, I. Y. (2002). Iron cycling and nutrient-limitation patterns in surface waters of the World Ocean. *Deep-Sea Research Part II*, *49*, 463–507. https://doi.org/10.1016/S0967-0645(01)00109-6

Moore, J. K., Doney, S. C., Kleypas, J. A., Glover, D. M., & Fung, I. Y. (2001). An intermediate complexity marine ecosystem model for the global domain. *Deep Sea Research Part II: Topical Studies in Oceanography*, *49*(1–3), 403–462. https://doi.org/10.1016/S0967-0645(01)00108-4

Moore, J. K., Doney, S. C., & Lindsay, K. (2004). Upper ocean ecosystem dynamics and iron cycling in a global three-dimensional model. *Global Biogeochemical Cycles*, *18*, GB4028. https://doi.org/10.1029/2004GB002220

Moore, J. K., Lindsay, K., Doney, S. C., Long, M. C., & Misumi, K. (2013). Marine ecosystem dynamics and biogeochemical cycling in the community earth system model CESM1(BGC): Comparison of the 1990s with the 2090s under the RCP4.5 and RCP8.5 scenarios. *Journal of Climate*, *26*(23), 9291–9312. https://doi.org/10.1175/JCLI-D-12-00566.1

Nagai, T., Gruber, N., Frenzel, H., Lachkar, Z., McWilliams, J. C., & Plattner, G.-K. (2015). Dominant role of eddies and filaments in the offshore transport of carbon and nutrients in the California Current System. *Journal of Geophysical Research: Oceans*, *120*, 5318–5341. https://doi.org/10.1002/2015JC010889

Omand, M. M., D'Asaro, E. A., Lee, C. M., Perry, M. J., Briggs, N., Cetinić, I., & Mahadevan, A. (2015). Eddy-driven subduction exports particulate organic carbon from the spring bloom. *Science*, *348*(6231), 222–225. https://doi.org/10.1126/science.1260062

Oschlies, A. (2002). Improved representation of upper-ocean dynamics and mixed layer depths in a model of the north Atlantic on switching from eddy-permitting to eddy-resolving grid resolution. *Journal of Physical Oceanography*, *32*(8), 2277–2298. https://doi.org/10.1175/1520-0485(2002)032<2277:IROUOD>2.0.CO;2

Oschlies, A., & Garçon, V. (1998). Eddy-induced enhancement of primary production in a model of the North Atlantic Ocean. *Nature*, *394*(6690), 266–269. https://doi.org/10.1038/28373

Pasquero, C. (2005). Differential eddy diffusion of biogeochemical tracers. *Geophysical Research Letters*, *32*, L17603. https://doi.org/10.1029/2005GL023662

Qin, X., Menviel, L., Sen Gupta, A., & van Sebille, E. (2016). Iron sources and pathways into the Pacific Equatorial Undercurrent. *Geophysical Research Letters*, *43*, 9843–9851. https://doi.org/10.1002/2016GL070501

Redi, M. H. (1982). Oceanic isopycnal mixing by coordinate rotation. *Journal of Physical Oceanography*, *12*(10), 1154–1158. https://doi.org/10.1175/1520-0485(1982)012<1154:OIMBCR>2.0.CO;2

Renault, L., Deutsch, C., McWilliams, J. C., Frenzel, H., Liang, J.-H., & Colas, F. (2016). Partial decoupling of primary productivity from upwelling in the California Current system. *Nature Geoscience*, *9*(7), 505–508. https://doi.org/10.1038/ngeo2722

Resplandy, L., Martin, A. P., Le Moigne, F., Martin, P., Aquilina, A., Mémery, L., et al. (2012). How does dynamical spatial variability impact 234th-derived estimates of organic export? *Deep Sea Research Part I: Oceanographic Research Papers*, *68*, 24–45. https://doi.org/10.1016/j.dsr.2012.05.015

Rintoul, S. R., & England, M. H. (2002). Ekman transport dominates local air–sea fluxes in driving variability of subantarctic mode water. *Journal of Physical Oceanography*, *32*(5), 1308–1321. https://doi.org/10.1175/1520-0485(2002)032<1308:ETDLAS>2.0.CO;2

Rohr, T., Long, M. C., Kavanaugh, M. T., Lindsay, K., & Doney, S. C. (2017). Variability in the mechanisms controlling Southern Ocean phytoplankton bloom phenology in an ocean model and satellite observations. *Global Biogeochemical Cycles*, *31*, 922–940. https://doi.org/10.1002/2016GB005615

Sallée, J.-B., Shuckburgh, E., Bruneau, N., Meijers, A. J. S., Bracegirdle, T. J., & Wang, Z. (2013). Assessment of Southern Ocean mixed-layer depths in CMIP5 models: Historical bias and forcing response. *Journal of Geophysical Research: Oceans*, *118*, 1845–1862. https://doi.org/10.1002/jgrc.20157

Siegel, D. A., Buesseler, K. O., Behrenfeld, M. J., Benitez-Nelson, C. R., Boss, E., Brzezinski, M. A., et al. (2016). Prediction of the export and fate of global ocean net primary production: The EXPORTS science plan. *Frontiers in Marine Science*, *3*, 22. https://doi.org/10.3389/fmars.2016.00022

Siegel, D. A., Buesseler, K. O., Doney, S. C., Sailley, S. F., Behrenfeld, M. J., & Boyd, P. W. (2014). Global assessment of ocean carbon export by combining satellite observations and food-web models. *Global Biogeochemical Cycles*, *28*, 181–196. https://doi.org/10.1002/2013GB004743

Small, R. J., Bacmeister, J., Bailey, D., Baker, A., Bishop, S., Bryan, F., et al. (2014). A new synoptic scale resolving global climate simulation using the Community Earth System Model. *Journal of Advances in Modeling Earth Systems*, *6*, 1065–1094. https://doi.org/10.1002/2014MS000363

Small, R. J., Curchitser, E., Hedstrom, K., Kauffman, B., & Large, W. G. (2015). The Benguela upwelling system: Quantifying the sensitivity to resolution and coastal wind representation in a global climate model. *Journal of Climate*, *28*(23), 9409–9432. https://doi.org/10.1175/JCLI-D-15-0192.1

Small, R. J., de Szoeke, S. P., Xie, S. P., O'Neill, L., Seo, H., Song, Q., et al. (2008). Air-sea interaction over ocean fronts and eddies. *Dynamics of Atmospheres and Oceans*, *45*(3–4), 274–319. https://doi.org/10.1016/j.dynatmoce.2008.01.001

Smetacek, V., Klaas, C., Strass, V. H., Assmy, P., Montresor, M., Cisewski, B., et al. (2012). Deep carbon export from a Southern Ocean iron-fertilized diatom bloom. *Nature*, *487*(7407), 313–319. https://doi.org/10.1038/nature11229

Smith, R. D., & Gent, P. R. (2004). Anisotropic Gent-McWilliams parameterization for ocean models. *Journal of Physical Oceanography*, *34*(11), 2541–2564. https://doi.org/10.1175/JPO2613.1

Smith, R. D., Jones, P., Bryan, F., Danabasoglu, G., Dennis, J., Dukowicz, J., et al. (2010). The Parallel Ocean Program (POP) reference manual (Tech. Rep. LAUR-10-01853). Los Alamos National Laboratory. Retrieved from http://www.cesm.ucar.edu/models/cesm1.0/pop2/doc/sci/POPRefManual.pdf

Song, H., Marshall, J., Gaube, P., & McGillicuddy, D. J. (2015). Anomalous chlorofluorocarbon uptake by mesoscale eddies in the Drake Passage region. *Journal of Geophysical Research: Oceans*, *120*, 1065–1078. https://doi.org/10.1002/2014JC010292

Song, H., Marshall, J., Munro, D. R., Dutkiewicz, S., Sweeney, C., McGillicuddy, D. J., & Hausmann, U. (2016). Mesoscale modulation of air-sea CO_2 flux in Drake Passage. *Journal of Geophysical Research: Oceans*, *121*, 6635–6649. https://doi.org/10.1002/2016JC011714

Stammer, D. (1997). Global characteristics of ocean variability estimated from regional TOPEX/POSEIDON altimeter measurements. *Journal of Physical Oceanography*, *27*(8), 1743–1769. https://doi.org/10.1175/1520-0485(1997)027<1743:GCOOVE>2.0.CO;2

Stukel, M. R., Aluwihare, L. I., Barbeau, K. A., Chekalyuk, A. M., Goericke, R., Miller, A. J., et al. (2017). Mesoscale ocean fronts enhance carbon export due to gravitational sinking and subduction. *Proceedings of the National Academy of Sciences of the United States of America*, *114*(6), 1252–1257. https://doi.org/10.1073/pnas.1609435114

Tagliabue, A., Aumont, O., DeAth, R., Dunne, J. P., Dutkiewicz, S., Galbraith, E., et al. (2016). How well do global ocean biogeochemistry models simulate dissolved iron distributions? *Global Biogeochemical Cycles*, *30*, 149–174. https://doi.org/10.1002/2015GB005289

Tagliabue, A., Sallée, J.-B., Bowie, A. R., Lévy, M., Swart, S., & Boyd, P. W. (2014). Surface-water iron supplies in the Southern Ocean sustained by deep winter mixing. *Nature Geoscience*, *7*(4), 314–320. https://doi.org/10.1038/ngeo2101

Turner, J. T. (2015). Zooplankton fecal pellets, marine snow, phytodetritus and the ocean's biological pump. *Progress in Oceanography*, *130*, 205–248. https://doi.org/10.1016/j.pocean.2014.08.005

Wang, C., Zhang, L., Lee, S.-K., Wu, L., & Mechoso, C. R. (2014). A global perspective on CMIP5 climate model biases. *Nature Climate Change*, *4*(3), 201–205. https://doi.org/10.1038/nclimate2118

Wang, Y., Olascoaga, M. J., & Beron-Vera, F. J. (2015). Coherent water transport across the South Atlantic. *Geophysical Research Letters*, *42*, 4072–4079. https://doi.org/10.1002/2015GL064089

Whitt, D. B., Lévy, M., & Taylor, J. R. (2016). Low- and high-frequency oscillatory winds synergistically enhance nutrient entrainment and phytoplankton at fronts. *Journal of Geophysical Research: Oceans*, *122*, 1016–1041. https://doi.org/10.1002/2016JC012400